REPORT DOCUMENTATION PAGE

AFRL-SR-BL-TR-00-

0529

1. AGENCY USE ONLY (Leave blank) --	2. REPORT DATE 7/00	3. REPORT TYPE AND DATES COVERED Final Technical 7/97–6/00

4. TITLE AND SUBTITLE	5. FUNDING NUMBERS
GaIn(As)P–GaAs Very Long Wavelength QWIP	F49620-97-1-0288

6. AUTHOR(S)

M. Razeghi

7. PERFORMING ORGANIZATION NAME(S) AND ADDRESS(ES)	8. PERFORMING ORGANIZATION REPORT NUMBER
Northwestern University Center for Quantum Devices 2225 N. Campus Drive Evanston, IL 60208-3129	

9. SPONSORING/MONITORING AGENCY NAME(S) AND ADDRESS(ES)	10. SPONSORING/MONITORING AGENCY REPORT NUMBER
Air Force Office of Scientific Research/NE 801 N. Randolph Street Arlington, VA 22203-1977	

11. SUPPLEMENTARY NOTES

20001023 050

12a. DISTRIBUTION/AVAILABILITY STATEMENT	12b. DISTRIBUTION CODE
Approved for public release; distribution unlimited	

13. ABSTRACT (Maximum 200 words)

A majority of infrared sensors used for imaging arrays operating in the long-wavelength infrared region between $\lambda = 8\text{-}12\ \mu m$ are based on HgCdTe. This material system structural difficulties due to poor uniformity, high defect densities, and weak bond strengths that cause difficulties in manufacturing large infrared focal plane array cameras. As an alternative, quantum well infrared photodetectors (QWIPs) utilizing intersubband absorption between GaAs wells and AlGaAs barriers were perfected. These QWIPs possess better uniformity in comparison to HgCdTe detectors, and QWIP imaging arrays have recently become commercially available. However, the responsivity of GaAs/AlGaAs QWIPs is still lower than HgCdTe detectors. In order to further improve the responsivity of QWIP detectors, the development of QWIPs with wells or barriers of GaInAsP instead of AlGaAs has been developed.

Results of detector characterization are presented for QWIPs fabricated from a variety of III-V material systems including GaAs/GaInP, GaInAs/InP, AlGaInAs/InP, and GaInAs/AlInAs. These material systems extend the range of sensitivity from 3-20 μm while remaining lattice-matched to InP. Also, lattice-matched multispectral detectors are demonstrated for sensitivity at both 4 μm and 8.5 μm. The ultimate objective is to produce a monolithically integrated QWIP focal plane array on Si substrate.

14. SUBJECT TERMS			15. NUMBER OF PAGES 62
			16. PRICE CODE

17. SECURITY CLASSIFICATION OF REPORT	18. SECURITY CLASSIFICATION OF THIS PAGE	19. SECURITY CLASSIFICATION OF ABSTRACT	20. LIMITATION OF ABSTRACT

Quantum Well Infrared Photodetectors

Project: F49620-97-1-0288
Project Manager: Major Dan Johnstone

End of Contract Report
June 2000

Principle Investigator: Dr. Manijeh Razeghi
Center for Quantum Devices, Northwestern University

Table of Contents

Executive Summary

A majority of infrared sensors used for imaging arrays operating in the long-wavelength infrared region between $\lambda = 8$–12 µm are based on HgCdTe. This material system is unable to satisfy all of the requirements that are imposed by modern applications. Structural difficulties due to poor uniformity, high defect densities, and weak bond strengths cause difficulties in manufacturing large infrared focal plane array cameras. As an alternative, quantum well infrared photodetectors (QWIPs) utilizing intersubband absorption between GaAs wells and AlGaAs barriers were perfected. These QWIPs possess better uniformity in comparison to HgCdTe detectors, and QWIP imaging arrays have recently become commercially available. However, the responsivity of GaAs/AlGaAs QWIPs is still lower than HgCdTe detectors. In order to further improve the responsivity of QWIP detectors, the development of QWIPs with wells or barriers of GaInAsP instead of AlGaAs has been developed.

Results of detector characterization are presented for QWIPs fabricated from a variety of III-V material systems. GaAs/GaInP QWIPs operating in the very-long wavelength infrared region are detailed. Extremely large responsivities of 33.2 AW^{-1} were obtained from GaInAs/InP QWIPs operating at $\lambda = 9$ µm which represents the largest value of responsivity for any QWIP in this wavelength range. Device parameters including carrier mobility, carrier lifetime, photoconductive gain, thermal generation rate, and carrier diffusion length are calculated from the experimental data. Devices made from AlGaInAs/InP and GaInAs/AlInAs have also been realized. These detectors extend the wavelength range of sensitivity from 3 µm out to 20 µm while remaining lattice-matched to InP. Lattice-matched multispectral detectors are demonstrated for sensitivity at both 4 µm and 8.5 µm.

Currently, there is limited knowledge about QWIPs based on material systems other than GaAs/AlGaAs. New QWIP designs intended to improve responsivity, especially designs developed to achieve multispectral detection, necessitate the use of more than one quantum well or barrier material. Also, the integration of III-V based QWIPs with Si-based readout integrated circuitry on Si substrate demands the precise and rigorous control of the quantum well absorption region that is placed under a strain of 8 % lattice mismatch.

1. Introduction

The ability to detect and process infrared radiation can provide a wealth of information about an object that is not available in other regions of the spectrum. One type of detector recently developed that can cover most of the infrared spectrum is the quantum well infrared photodetector (QWIP). By using intersubband absorption within a quantum well, a QWIP can be designed with relatively wide-bandgap materials yet be sensitive to low-energy photons in the infrared.

Since infrared absorption due to intersubband transitions was first observed in multiple quantum well (MQW) structures,[1] quantum well infrared photodetectors (QWIPs) and arrays based on this principle have become a competitive infrared technology.[2] Because of the extensive scientific and commercial exploration of the AlGaAs/GaAs material system over the past decades, the application of this technology to QWIPs has rapidly reached commercial maturity.

QWIPs also have been fabricated from numerous alternative III-V material systems, including GaAs/GaInP, GaInAs(P)/InP, and (Al)GaInAs/InP. Table 1 shows three material systems and some of their properties from which QWIPs in the $\lambda = 8$–9 μm range have been demonstrated. Better results have been achieved with the GaInAs/InP material system since it offers a higher well and barrier mobility, lower well electron effective mass, and a binary barrier with a inherently lower defect density.[3,4,5,6]

Table 1. Properties of commonly used material systems for QWIP fabrication in the $\lambda = 8$–9 μm range.

Material system	GaAs/AlGaAs	GaAs/GaInP	GaInAs/InP
Barrier material	AlGaAs (ternary)	GaInP (ternary)	InP (binary)
Well mobility, 300 K ($cm^2V^{-1}s^{-1}$)	9000	9000	13 500
Barrier mobility, 300 K ($cm^2V^{-1}s^{-1}$)	2000	3500	5500
Well electron effective mass (m^*/m_0)	0.067	0.067	0.041

Another disadvantage of GaAs/AlGaAs QWIPs is that perpendicular carrier transport rapidly degrades when the $Al_xGa_{1-x}As$ barrier becomes indirect gap (for x > 0.45). For this reason, the shortest wavelength infrared detector possible with this material system is ~ 6 μm.[7] Thus, the need to achieve mid-wavelength absorption has lead to studies of other material systems such as $In_{0.2}Ga_{0.8}As/Al_{0.38}Ga_{0.62}As$,[8] and $In_{0.53}Ga_{0.47}As/Al_{0.48}In_{0.52}As$.[9] These material systems avoid the use of indirect gap AlGaAs barriers.

For some applications, especially for tunneling devices, $In_{0.53}Ga_{0.47}As/Al_{0.48}In_{0.52}As$ MQWs lattice-matched to InP substrates have several advantages in comparison to structures composed of $InGaAs/Al_xGa_{1-x}As$, where x is small enough to ensure a direct energy gap in the AlGaAs barrier material: (1) The effective mass of the electrons, which governs the drift mobility and tunneling properties, amounts to $0.041 \cdot m_0$ in InGaAs as compared to $0.053 \cdot m_0$ in $In_{0.2}Ga_{0.8}As/AlGaAs$, where m_0 is the free-electron mass. (2) The MWIR InGaAs/AlInAs quantum well detector is lattice matched with LWIR InGaAs/InP QWIP detectors, allowing a 2-color lattice-matched detector stack to be grown on InP. The InGaAs/AlGaAs QWIP is strained

7% to GaAs, which introduces dislocations into the growing layer and degrades its performance and that of the subsequent LWIR GaAs/AlGaAs detector.

The demand for automatic target detection, definition, and recognition is mandating the development of dual wavelength forward looking infrared (FLIR) sensor arrays. Two-color infrared detectors designed for dual band applications require mid-wavelength infrared (MWIR) and long-wavelength infrared (LWIR) focal plane arrays to be monolithically integrated on a single substrate. This objective has been difficult to achieve due to the lattice mismatch between commonly used interband MWIR and LWIR infrared materials such as InSb and HgCdTe. For this reason, stacks of lattice-matched multi-quantum well intersubband photodetectors have been proposed for use in multi-color infrared detectors.

The ultimate objective is to produce a monolithically integrated GaInAs/InP QWIP focal plane array on Si substrate. There are many benefits for directly growing III-V detectors, such as QWIPs, on Si substrates: Si substrates are cheaper, come in larger sizes, and have greater mechanical strength and higher thermal conductivity. Additionally, the direct integration of III-V detectors and Si readout circuitry would result in simpler fabrication and lower-cost focal plane arrays. But due to the differences in lattice constant and thermal expansion between InP and Si or even GaAs and Si, growth on Si substrates is more difficult. Methods must be developed that will produce QWIPs directly on Si with satisfactory performance.

2. Overview of QWIPs

Interestingly, despite the long history of infrared detectors, QWIPs have only recently emerged on the scene. The idea of using quantum wells for infrared detection was first presented by Esaki and Sakaki in 1977.[10] Eight years later, West and Eglash made the first experimental observations of strong intersubband absorption in a multi-quantum well structure.[1] Finally, a couple of years later in 1987, the first QWIP device based on intersubband absorption was demonstrated by Levine et al.[11] Since that time, QWIP technology has developed rapidly to the point that it has reached commercial maturation in the summer of 1999.[12]

2.1. Applications of infrared detectors

The greatest scientific and technological impact of the development of infrared detectors has been in infrared astronomy, environmental remote sensing, and industrial process control. For example, by looking at infrared emission across different spectral wavelengths, earth observation satellites can monitor the development of storms, plant dehydration or saturation, crop types, and other important ecological parameters. Astronomers examine the far reaches of the universe in the infrared in order to detect objects that are too cold to emit light visible to the human eye. In addition, infrared detectors have played a revolutionary role in modern warfare. Since infrared imaging does not rely on reflected visible light, it offers the possibility of "seeing" in the dark or through obscured conditions by detecting the infrared energy emitted by objects.

Fig. 1 demonstrates such an application. Both images were captured by a television news helicopter flying over Malibu, California during a period when hillside fires were burning through the city.[13] The images were taken at night of an area that had just burned. Fig. 1(a) was taken with a visible CCD camera, and between the nighttime conditions and the smoke, the image appears pitch black. Fig. 1(b) was taken with a QWIP infrared focal plane array (FPA) camera, and the terrain below is clearly visible. The white splotches are hot spots that have still lingered and could possibly flare up again. These only become apparent when imaging in the infrared.
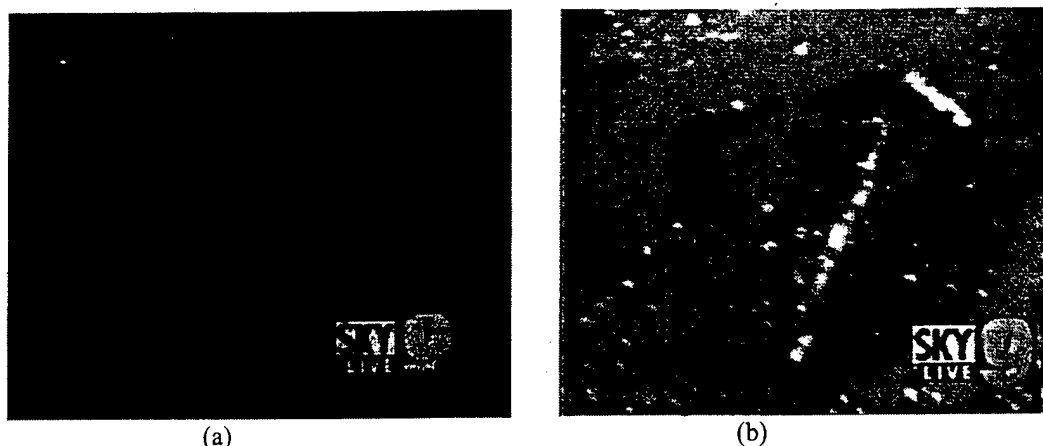
Fig. 1. Images captured with (a) a visible CCD camera and (b) an infrared QWIP camera by a television news helicopter flying over Malibu, California during a period when hillside fires were burning through the city. The images were taken at night of an area that had just burned. The white splotches in (b) are hot spots that have still lingered and could possibly flare up again.

2.2. Types of infrared detectors

Any photodetector, whether it is a pollution sensor, a satellite-mounted space imager, or the human eye, must be able to absorb incident radiation and give off a measurable signal based on the intensity of radiation absorbed. For the case of infrared detectors, there are two basic types: thermal detectors and photon detectors. The difference between the two is how incident light affects the absorbing material.

2.2.1. Thermal detectors

In thermal detectors, absorbed light elevates the temperature of the material, which in turn alters another physical property. The change in the physical property can be sensed and a signal can be generated. Thermal detectors have a wavelength-independent sensitivity, a relatively slow response, and can operate up to room temperature.

The first advancement after the mercury-bulb thermometer was the thermopile, which took advantage of the thermoelectric effect. This states that when two different metals are joined together—forming a thermocouple—and the two ends of the thermocouple are at different temperatures, a voltage will result that is proportional to the temperature difference. The sensitivity was increased by using many thermocouples in series.

The Golay pneumatic detector, or Golay cell, consists of a small volume of gas in contact with a thin metal film. The metal film absorbs light and heats up, and the heat is transferred to the gas. The resultant pressure increase changes the angle of a mirror inside the cell, which alters the path to an optical amplifier.

The absorbing material within a pyroelectric detector undergoes a change in dielectric constant with a change in temperature. The pyroelectric material is contained inside a voltage-biased capacitor which acts as a source of current that is proportional to the time rate of change of the material's dielectric constant. A bolometer experiences a change in electrical resistance with temperature; thus the amount of current that can pass through it is proportional to temperature.

5

The bulk of the research done today in the field of thermal detectors is for pyroelectric detectors and bolometers. Most of the recent research in pyroelectric materials has been in high-temperature superconducting materials, including YBaCuO[14] and PbLaTiO$_3$.[15] Large bolometer detector arrays have successfully been constructed with vanadium oxide deposited on micro-machined Si wafers,[16] though in this area as well, much attention is focused on the superconductors YBaCuO[17] and GdBaCuO.[18] As long as wavelength selectivity is not required, thermal detectors give unsurpassed performance for operating temperatures above 77 K.[19]

2.2.2. Photon detectors

In photon detectors, absorbed light excites electrons into a higher energy state, and these electrons can be sensed before they relax. Because the method of detection is different than in thermal detectors, photon detectors have a non-uniform spectral response. Additionally, they generally have extremely fast operation and some work up to room temperature. Photon detectors can be divided into four groups: photoeletric, extrinsic semiconductor, intrinsic semiconductor, and quantum well detectors.

The photoelectric or Schottky-barrier detector consists of a very thin metal coating a doped semiconductor, thus forming a Schottky barrier. For the case of an n-type Si semiconductor in contact with a metal, the Fermi level of the semiconductor aligns with the Fermi level of the metal, forming a potential barrier at the metal-semiconductor interface. This is shown in Fig. 2.
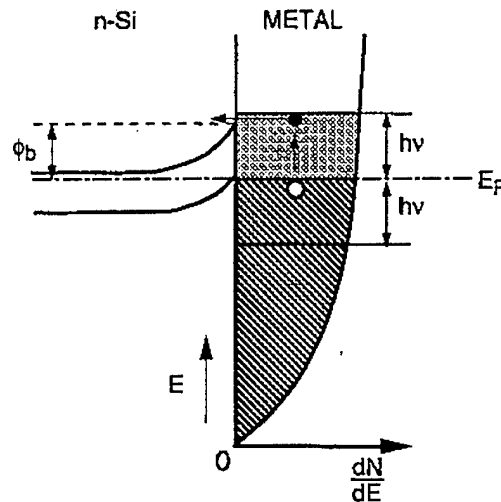

Fig. 2. A Schottky barrier for the case of an n-type Si semiconductor in contact with a metal. In a photoelectric detector, only those excited electrons in the metal with sufficient energy pass over the barrier into the semiconductor, where they are collected and measured.

Incident photons are absorbed in the metal layer and create electron-hole pairs. The excited electrons randomly transport in the metal, until they reach the metal-semiconductor interface. Only those electrons with sufficient energy pass over the barrier into the semiconductor, where they are collected and measured.

Photoelectric detectors are capable of a broad response spectrum, depending on the type of metal coating used. Very large 1040×1040 arrays have been made with PtSi metal on a p-type Si substrate with a cutoff squarely in the MWIR.[20] Additionally, a bi-spectral 811×508 PtSi

detector with detection in the ranges 1.5–2.5 µm and 3–5.5 µm has recently been constructed.[21] The cutoff-wavelength can be extended into the LWIR by using IrSi as the coating metal.[22]

Extrinsic semiconductor detectors are made from a bulk Si or Ge crystal doped with a single type of impurity. The energy gap of the bulk crystal is too large for detection above 2 µm, however, the addition of the impurities adds a new allowable level in the energy gap. Fig. 3 displays the impurity energy level inside the crystal's bandgap. Electrons at the impurity level only need to be excited with an energy larger the impurity activation energy, and upon reaching the conduction band they can be collected and measured.
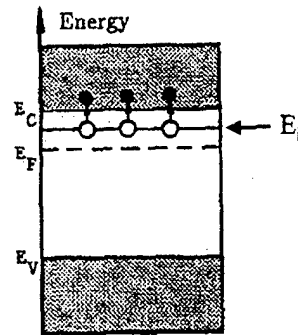

Fig. 3. The impurity energy level of an extrinsic semiconductor detector. Electrons at the impurity level only need to be excited with an energy larger the impurity activation energy, and upon reaching the conduction band they can be collected and measured.

Since the activation energy of an impurity is very small, the cutoff wavelengths that are possible exceed 100 µm. This also implies that a very low operating temperature is required, because to avoid excessive thermally generated carriers, the detector must be operate at a temperature T such that the thermal activation energy kT is less than the impurity activation energy. The most common extrinsic semiconductor detector material is Si:Ga, which has a cutoff wavelength of 18.4 µm, making it very useful for space-based applications despite its maximum operating temperature of ≈ 10 K.[23]

Intrinsic semiconductor detectors differ from extrinsic ones in that an excited electron must cross the entire bandgap to reach the conduction band. This is illustrated in Fig. 4. Therefore, for infrared detection in the MWIR or LWIR regions, narrow-gap semiconductors must be used. The detectors can be either photoconductive or photovoltaic. For photoconductive detectors, an excited electron is transported through the semiconductor under an external bias and contributes to the photocurrent. For photovoltaic detectors, incident photons generate an electron-hole pair inside a p-n junction, and the carriers get swept to opposite sides of the junction, creating an internal bias.

absorbed photon ➡

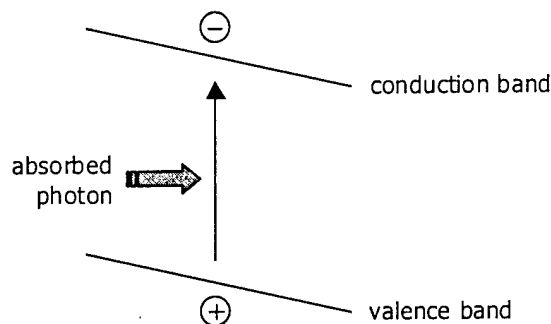⊖ conduction band

⊕ valence band

Fig. 4. Intrinsic semiconductor detectors differ from extrinsic ones in that an excited electron must cross the entire bandgap to reach the conduction band.

The narrow-gap semiconductors that have been used are the IV-VI, II-VI, and III-V alloys, some of which approach being a semi-metal, meaning that the bandgap approaches zero. The IV-VI binaries PbS and PbSe were extensively developed during World War II and the following decade for low-cost detection in the SWIR and MWIR ranges. With the use of the ternaries PbSnTe and PbSSe, the detection range could be extended into the LWIR.[24] The material technology for these systems have been well developed, however, they suffer from a relatively large dielectric constant and too high a thermal coefficient of expansion, fundamental constraints that place a limit their performance.

The most popular material for infrared detection has since been the II-VI alloys, chiefly HgCdTe. Because of the extensive research performed on HgCdTe, it is the standard against which all other IR photon detectors are matched up to. Compared with the IV-VI alloys, HgCdTe offers the ability to dope in both low and high concentrations, has high electron mobility, and a small change in lattice constant with change in composition.

Where HgCdTe shines is its quantum efficiency and detectivity: at 77 K, quantum efficiency has been reported exceeding 70% and detectivity exceeding 10^{12} $cmHz^{1/2}W^{-1}$.[25] FPAs as large as 640×480 have been made that can detect either in the MWIR or LWIR region and are compatible with Si readout circuitry.[26] A dual-color 128×128 FPA has been demonstrated that is simultaneously sensitive to two bands in the MWIR.[27] The array was constructed by using an n-p-n junction, which in effect is two p-n junctions placed back-to-back. A similar dual-color 64×64 FPA has also been demonstrated that is simultaneously sensitive to the MWIR and LWIR.[28]

Despite these results, a serious problem exists with the alloy that makes the production of HgCdTe detectors troublesome. While the fundamental properties of the material is favorable, the technology of producing HgCdTe material and detectors is far from reliable. HgCdTe, as an alloy, is not stable: there is a segregation of the constituent binaries during crystallization and the bonding between Hg and Te is weak, facilitating defect formation and Hg migration. The uniformity and reproducibility of a HgCdTe film is poor,[29] and passivation is required to process detectors. The end result of using this material is low-yield and high-cost detector arrays.

This motivates the search for alternative material systems. The III-V intrinsic semiconductor detectors are one such option. The III-V alloys offer a high bond strength and better material stability than II-VI alloys, plus they offer the ability to grow on widely-available III-V substrates. InSb is a heavily investigated material with detection in the MWIR region, while the ternaries InAsSb,[30] InBiSb,[31] and InTlSb[32] can extend detection in the LWIR region

with room-temperature operation. The largest obstacle to overcome with these materials is the large lattice mismatch they have with their host substrate.

The other major alternative is a different breed of detector: the quantum well infrared photodetector (QWIP).[7,33] QWIPs are constructed from quantum wells of wide-bandgap materials that in bulk do not absorb in the MWIR or LWIR. However, since quantum wells are used, electron excitation may occur between two energy levels *within* the quantum well, making absorption possible in the MWIR or LWIR regions.

2.3. Intersubband absorption

As mentioned in the previous section, a traditional intrinsic semiconductor photon detector is only sensitive to photons whose energy is larger than the semiconductor's bandgap. Thus, for detection in the MWIR or LWIR regions of the spectrum, a narrow bandgap material must be used. The mechanism of exciting a carrier from the valence band directly to the conduction band is called *interband* absorption, which is shown in Fig. 4.

To take advantage of the superior material growth and technology that exists with the wide bandgap materials, such as AlGaAs/GaAs or GaInAs/InP, a diffrerent mechanism is employed for detection in the MWIR or LWIR. While interband absorption in these materials occurs only in the SWIR or visible regions of the spectrum, *intersubband* absorption, through the use of quantum wells, can make longer-wavelength detection possible. The process is shown in Fig. 5.
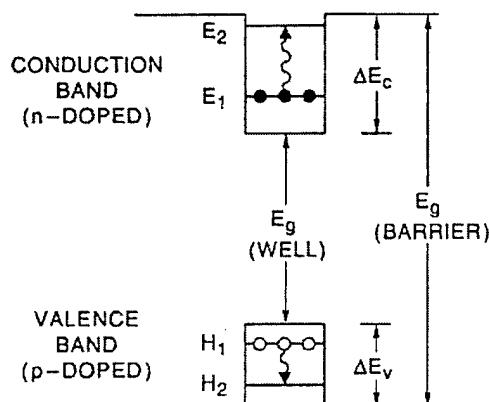

Fig. 5. Intersubband absorption, which takes place entirely within the valence band (H_1 to H_2) or conduction band (E_1 to E_2) of a quantum well.

The quantum well consists of a very thin layer, less than 100 Å, of smaller bandgap material (the well), sandwiched by a larger bandgap material (the barrier). This produces a "particle-in-the-box" phenomenon where the allowed energy states inside the well are confined to bound levels. Absorption takes place from one bound level in the quantum well to another, as seen in Fig. 2.5. The energy separation between the two bound levels, E_1 and E_2 or H_1 and H_2, is much smaller than the bandgap of either the well or barrier material, hence the intersubband absorption wavelength is much longer.

One requirement for detection using quantum wells is that the well material must be doped. Because the energy of an absorbed photon is less than the bandgap, it cannot produce an excited photocarrier by itself. With the addition of carriers in the well, excitation only needs to happen from the first bound state to the next bound state. For *n*-type doping, excitation occurs

entirely within the conduction band; for p-type doping, excitation occurs entirely within the valence band.

The integrated absorption strength of a multi-quantum well structure is given by

$$\int_0^\infty \alpha(v)dv = \left(\frac{\rho_c N_w q^2 hf}{4\varepsilon_0 m^* c n_r}\right)\left(\frac{\sin^2\theta}{\cos\theta}\right) \tag{1}$$

where $\alpha(v)$ is the absorption spectrum, v is the frequency, $\rho_c = N_D L_w$ is the two-dimensional carrier density in the well, N_D is the three-dimensional carrier density, L_w is the well thickness, N_w is the number of doped wells in the structure, q is the charge of an electron, h is Planck's constant, f is the oscillator strength, ε_0 is the permittivity of free space, m^* is the electron effective mass in the well, c is the speed of light, n_r is the refractive index of the well material, and θ is the angle between the incident light and direction perpendicular to the quantum wells.

The oscillator strength f is proportional to the square of the optical matrix element $<z>$, where z represents the direction perpendicular to the quantum wells. This, along with the fact that the absorption strength is proportional to $\sin^2\theta/\cos\theta$, implies a serious constraint of quantum well absorption: the electric field of the incident light must have a component parallel to z in order for absorption to occur. Therefore the direction of the incident light cannot be normal to the quantum wells—when $\theta = 0°$—and must come in at an angle. Fig. 6 shows the absorbance as a function of incidence angle. The peak at $\theta = 73°$ corresponds to the Brewsters' angle, and the decrease in absorbance with decreasing incidence angle is readily seen. Methods used to accommodate the oblique incidence are discussed later in the section.
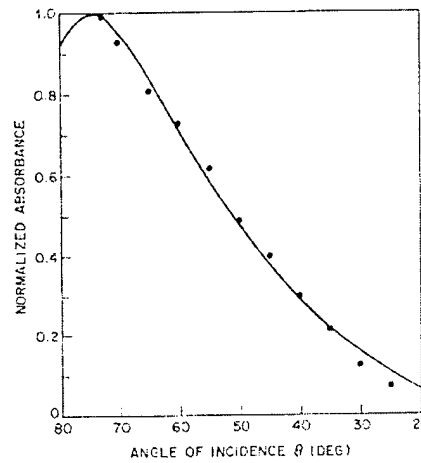

Fig. 6. The absorbance as a function of incidence angle in a QWIP. The peak at $\theta = 73°$ corresponds to the Brewsters' angle.

One remarkable note is that this quantum mechanical selection rule for absorption only applies to quantum wells that are doped n-type. For p-type quantum wells, there is strong mixing amongst the heavy holes and light holes in the valence band which can make absorption of normal incidence light possible.[34]

Photocurrent is produced when an excited photocarrier is able to escape the well whereupon an externally applied bias can sweep it out to be collected by one of the contacts. Based on the properties of the quantum well, like the well thickness and depth, the absorption

10

spectrum can tailored for detection at a particular range of wavelengths. Based on this information, the reasoning for the name *quantum well infrared photodetector* (QWIP) becomes evident.

2.4. Types of intersubband absorption

The first type of QWIPs produced had intersubband absorption occurring between two bound states contained within the quantum well, similar to the levels E_1 and E_2 shown in Fig. 5. In this case, when the quantum well contains two or more bound states, the QWIP is known as a *bound-to-bound state* QWIP.

When a carrier absorbs a photon and jumps up to the second bound state, it still needs a way to escape from the well and get swept out. The two possible ways are shown in Fig. 7. The first is by tunneling through the barrier, and the second is by thermionic emission, where the carrier is thermally excited out of the well. For a bound-to-bound state QWIP, tunneling usually dominates, and this only happens when the applied electric field is sufficiently large.
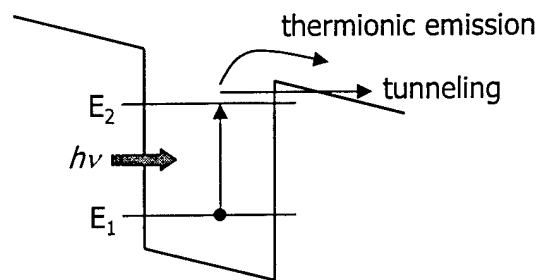

Fig. 7. A bound-to-bound state transition, showing the two possible ways a photocarrier can escape the well: tunneling and thermionic emission.

A serious problem that has been experienced with bound-to-bound state QWIPs is the excessive amount of dark current generated in the detector. The same mechanisms that produce photocurrent in a bound-to-bound state QWIP, tunneling and thermionic emission, can also produce dark current. The difference is that dark current is created in the absence of photon absorption.

It relates to the structure of a bound-to-bound state QWIP. Since the bulk of the photocarriers tunnel out of the quantum well, it is advantageous to have thinner barriers to facilitate tunneling. Additionally, a large electric field is needed for tunneling to occur at a tolerable rate. The combination of these two factors more easily allows random carriers in the well to also tunnel out, producing a relatively large dark current.

The way to circumvent this is to have the excited photocarriers escape the quantum well without tunneling. By making the quantum wells thinner, the energy level of the second bound state is raised enough so that it is completely out of the well and into the continuum band. When a carrier becomes excited, it jumps from the first bound state in the well to the contiuum state above the well. Once there, it is readily swept out.

The bound-to-continuum transition is shown in Fig. 8. The barriers can be much thicker in this type of structure, which dramatically reduces the dark current. Also, the large electric field required in the bound-to-bound state QWIP is no longer needed, further reducing the dark current. In this case, when the quantum well contains only one bound state, the QWIP is known as a *bound-to-continuum state* QWIP.
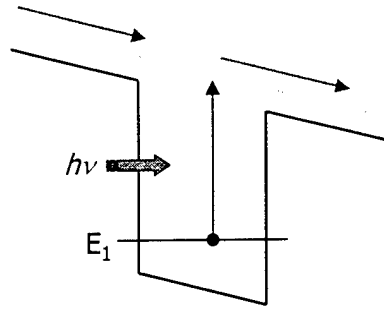
11

Fig. 8. A bound-to-continuum state transition.

It has been found experimentally that thicker barriers can decrease the dark current. For example, when the barrier thickness was increased from 300 Å to 480 Å in a 10 μm GaAs/AlGaAs QWIP, the dark current was reduced by one order of magnitude.[35] Also, the dark current is reduced by lowering either the bias or the temperature, naturally. For temperatures greater than ≈45 K, the QWIP dark current is dominated by thermionic emission. Below that, it is dominated by tunneling from well to adjacent well.[36]

While a bound-to-continuum state QWIP has been shown to have a smaller dark current than a bound-to-bound state QWIP, it has a much broader absorption spectrum. This is demonstrated in Fig. 9 for three GaAs/AlGaAs QWIPs grown and processed under the same conditions.[37] The intersubband transition in a bound-to-bound state QWIP takes place between two sharply defined energy levels in the well. Its absorption spectrum, then, is expected to be narrow. In the graph below, the peak width $\Delta\lambda/\lambda$ of the bound-to-bound state QWIP is only 9% (calculated by taking the full width at half maximum and dividing by the peak wavelength).
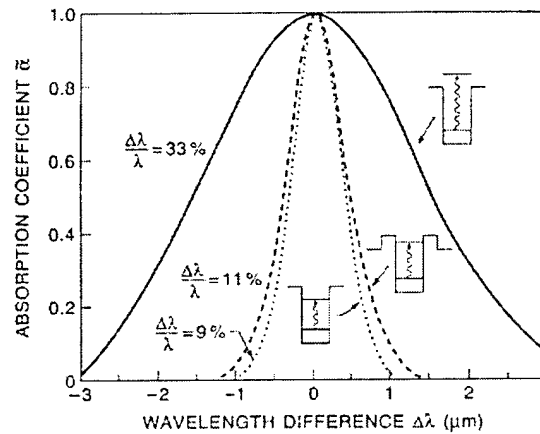

Fig. 9. A comparison of the absorption spectra of three GaAs/AlGaAs QWIPs, each with its own type of intersubband transition.

The transition in the bound-to-continuum state QWIP takes place between a sharply defined energy level in the well and a broad continuum band above the well. Its absorption spectrum is expected to be wider, and in the case of the sample above, the peak width $\Delta\lambda/\lambda$ = 33%. The only difference between this sample and the bound-to-bound sample is the GaAs well thickness, which was decreased from 50 Å to 40 Å; the well doping concentration and the AlGaAs barrier thickness and composition remained the same.

12

The third sample shown is a bound-to-quasibound state QWIP. It has the exact same parameters as the bound-to-continuum state QWIP, except for the insertion of two thin barriers of higher bandgap on either side of the well. The second energy level is now bound within the two thin barriers, which narrows the absorption spectrum down to $\Delta\lambda/\lambda = 11\%$, almost the same value as the bound-to-bound state QWIP.

2.5. QWIP parameters

The photocurrent I_p generated in a QWIP can be written as

$$I_p = n_p q v \tag{2}$$

where n_p is the volume density of photogenerated carriers and v is the transport velocity through the QWIP. n_p is given by

$$n_p = \frac{P \cos\theta\, \alpha}{h\nu} p_e \tau_L$$

where P is the incident optical power on the detector, p_e is the escape probability from the quantum well, and τ_L is the recapture lifetime.

From this information we can calculate the detector's responsivity, which is defined as the ratio of the electrical current generated by the detector to the total optical power absorbed. Expressed mathematically, the peak responsivity R_p—the maximum value of responsivity as a function of photon energy—is

$$R_p = \frac{I_p}{P \cos\theta} = \frac{q}{h\nu}\eta_a p_e g \tag{3}$$

where η_a is double-pass absorption quantum efficiency and g is the photoconductive gain. Given the length of the multi-quantum well region as l, η_a and g are defined as

$$\eta_a = \frac{1 - \exp(-2\alpha l)}{2} \tag{4}$$

and

$$g = \frac{v\tau_L}{l} = \frac{\tau_L}{\tau_T} = \frac{L}{l} \tag{5}$$

where $\tau_T = l/v$ is the transit time and L is the hot electron mean free path. The overall quantum efficiency η is calculated as

$$\eta = \eta_a p_e = \frac{R_p h\nu}{qg} \tag{6}$$

13

This gives an indication of how many carriers are being generated, which may contribute to the photocurrent, versus how many photons are absorbed.

The other type of current in a QWIP, the dark current, can be calculated from

$$I_d(V) = n^*(V)qv(V)A \tag{7}$$

where $n^*(V)$ is the effective number of electrons excited from the well into the continuum state, $v(V)$ is the average transport velocity, and A is the detector area. $n^*(V)$ is expressed as

$$n^*(V) = \frac{m^*}{\pi\hbar^2 L_p} \int_{E_1}^{\infty} f(E)T(E,V)dE \tag{8}$$

where L_p is the superlattice period, $T(E,V)$ is the tunneling current transmission factor for a single barrier, and $f(E)$ is the Fermi factor, given by

$$f(E) = \frac{1}{1 + \dfrac{\exp(E - E_1 - E_F)}{kT}}$$

where E_F is the two-dimensional Fermi level, k is Boltzmann's constant, and T is the temperature. The average transport velocity $v(V)$ is given as

$$v(V) = \frac{\mu F}{\sqrt{1 + \left(\dfrac{\mu F}{v_s}\right)^2}}$$

where μ is the mobility, F is the average electric field, and v_s is the saturated drift velocity.

Related to the dark current is the noise current, which ultimately becomes the limiting factor for the sensitivity of a detector: the signal (responsivity) of a detector can be externally amplified, but the noise current would be amplified in kind, leaving the signal to noise ratio unchanged. Several kinds of noise have been identified in photodetectors, though there are just two that can dominate the noise current in a QWIP.[38]

The first is called generation-recombination noise, or GR noise. It is composed of random thermal excitation and decay of carriers in the quantum wells, leading to fluctuations in the number of carriers. The second is Johnson noise, which is a strictly thermal noise, and causes fluctuations in the velocity of carriers. Since noise is a random process, the addition of noises obeys the root mean square (rms) system, that is, the square of the total noise equals the sum of the squares of the component noises. The total noise current i_n in a QWIP, then, is

$$i_n^2 = i_{GR}^2 + i_{Johnson}^2$$

The GR noise current and the Johnson noise current are given by

$$i_{GR} = \sqrt{4qI_d g\Delta f} \qquad (9)$$

and

$$i_{Johnson} = \sqrt{\frac{4kT}{R}} \qquad (10)$$

where Δf is the measurement bandwidth and R is the series resistance of the QWIP.

Lastly, the specific detectivity gives the signal to noise ratio of the detector. As discussed earlier, it is an indication of how small a signal a detector can pick up. The specific detectivity D^* is given by

$$D^* = \frac{R_p \sqrt{A\Delta f}}{i_n} \qquad (11)$$

It is a standardized figure of merit for both photovoltaic and photoconductive detectors and is independent of detector area or peak absorption wavelength.

2.6. QWIPs v. HgCdTe

If QWIPs wish to become a viable detector technology and have any chance of commercial success, it must dethrone HgCdTe as the better choice for infrared detection—at least for some applications. This is no easy task: HgCdTe has been, by far, the most studied material for detector applications over the last three decades. No other material system comes close.

As stated in Sec. 2.2.2, HgCdTe is a II-VI material system. It posseses excellent fundamental material properties, and its direct interband transition gives it a big advantage in quantum efficiency. For a single detector operating at temperatures above 70 K, its specific detectivity is unsurpassed. Yet, as also stated in Sec. 2.2.2, it has notoriously poor material growth and processing. The instability of the alloy leads to excessive defect formation and unreliable material uniformity and reproduciblility. The alloy is soft and brittle, making it difficult to process, and the presence of surface leakage current and inferior thermal properties necessitate the use of passivation during processing. As a result, the progress in developing HgCdTe FPAs has been slow.

QWIPs, by contrast, use the III-V material system, which is very mature due to the previous development of GaAs- and InP-based lasers, light emitting diodes, and microwave circuitry. The growth and fabrication of QWIPs can be borrowed directly from these technologies. Yet the intersubband transition gives the QWIP a quantum efficiency of only ≈10%, much smaller than for HgCdTe. QWIPs also have a higher thermal generation rate than HgCdTe detectors, which further decreases their detectivity. Another aspect is that the intersubband transition gives the QWIP a much sharper absorption spectrum, since only those photons with energies near the allowed transition energy are absorbed, while any photon with an energy larger than the bandgap gets absorbed in the interband HgCdTe detector.

The fundamental advantages of HgCdTe get wiped out when the operating temperature is decreased to under ≈50 K, because in this regime the quality of the material comes strongly into

15

play. For low biases and temperatures above 60 K, the main mechanism of dark current in HgCdTe is diffusion current. Below 50 K, tunneling current related to localized defects becomes dominant.[25] The large amount of defects present in the HgCdTe material can directly lead to excessively high dark current. In QWIPs below 45 K, defect-related tunneling dominates the dark current. Since QWIPs are composed of III-V material with a much lower defect density, its dark current can be comparably lower at these temperatures.

The extension of the cutoff wavelength to the VLWIR poses more problems for HgCdTe. Fig. 10 displays the cutoff wavelength in a HgCdTe detector at 77 K as a function of composition. For the MWIR, there is small variation in wavelength versus composition. However, as one moves to the LWIR and especially the VLWIR, the cutoff wavelength is extremely sensitive to the composition. As shown in the figure, when the percentage of CdTe x in $Hg_{1-x}Cd_xTe$ is 0.199, the cutoff wavelength is 14 μm. When x is decreased slightly to 0.184, the cutoff wavelength jumps to 20 μm. Given the difficulty in controlling the composition of HgCdTe, controlling the cutoff wavelength in the VLWIR becomes incredibly intricate.
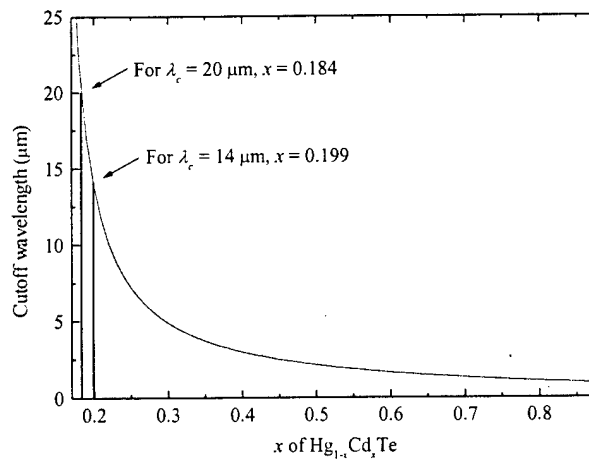

Fig. 10. The cutoff wavelength in a HgCdTe detector at 77 K as a function of composition. As one moves to the LWIR and especially the VLWIR, the cutoff wavelength is extremely sensitive to the composition.

QWIPs avoid this problem because the cutoff wavelength is less sensitive to the properties of the quantum well, like the well depth and thickness, than it is to composition of an intrinsic semiconductor. Furthermore, extension of QWIPs to the VLWIR is straightforward: the material properties, growth, and processing are identical for a VLWIR QWIP as for a LWIR QWIP. This is not the case for HgCdTe.

Another advantage of QWIPs based on the III-V material system is its radiation hardness. When a material is used in outer space, it is bombarded with cosmic radiation that can knock atoms out of lattice positions and degrade detector performance. If a material can withstand this extraterrestrial onslaught without suffering significant loss of performance, its radiation hardness is good. III-V materials have good radiation hardness; II-VI materials do not.

The next major issue is scalability from a single detector to a large-area array. Virtually all infrared detector applications, notably target identification, discrimination, or tracking, require FPAs. This raises new concerns for detector peformance, since the FPAs can contain hundreds of thousands of individual detectors. One of the most important is pixel operability, which tells what percentage of detectors from the array operate within a specified tolerance.

16

The proclivity of material defects in HgCdTe results in a large number of bad pixels. This can be fatal to an array, especially when bad pixels are adjacent to one another, since it can lose track of a target as it registers across the array field of view. HgCdTe FPAs also have a larger pattern noise than QWIP FPAs. Pattern noise is a result of the local variation of dark current, photoresponse, and cutoff wavelength, and is a major limitation of array performance. Again, this is due to the superior material quality and control of cutoff wavelength in QWIPs.

Another advantage of QWIP FPAs is in integration time. This is the amount of time charge is collected in the read-out capacitor of each pixel; a longer integration time means lower noise. Because HgCdTe has a lower R_0A product (device resistance times area), more current will flow from each pixel. This usually saturates the read-out capacitor, and the only way to avoid this problem is to reduce the integration time. A QWIP detector, with its much larger R_0A product, can have a significantly longer integration time.

Table 2 gives a comparison of recently reported HgCdTe and QWIP FPAs in both the LWIR and VLWIR by Rockwell, JPL, and Lockheed Martin.[39] The QWIPs were all made with GaAs/AlGaAs. For cutoff wavelengths in both the LWIR and VLWIR, the HgCdTe FPAs have a higher operating temperature, but the QWIP FPAs have the longer integration time and better operability.

Table 2. A comparison of recently reported HgCdTe and QWIP FPAs in both the LWIR and VLWIR by Rockwell, JPL, and Lockheed Martin.

Parameter	HgCdTe (Rockwell)	QWIP (JPL)	QWIP (Lockheed Martin)	HgCdTe (Rockwell)	QWIP (JPL)
Array size	256×256	256×256	640×480	128×128	128×128
Wavelength range (μm)	1–10.5	8.0–9.0	8.5–9.5	1–13.8	13.2–15.0
Operating temperature (K)	77	72	60	60	45
F/#	3.8	2.0	2.3	3.8	2.3
NEΔT (mK)	20	15	15–25	44	15
Integration time (ms)	0.468	10	4	0.067	15
Operability (%)	99.65	99.99	99.99	99.33	99.99
Pitch (μm)	40	38	24	40	50
Fill factor (%)	100	54	84	100	54
Raw non-uniformity (%)	4.9	2.0	5	9.2	2.0
Corrected non-uniformity (%)	0.019	0.01	0.1	n/a	0.01
Background (photons·cm^{-2}s^{-1})	4.1×10^{15}	7×10^{15}	6.3×10^{15}	8.2×10^{15}	9×10^{15}
Detectivity (cmHz$^{1/2}$W^{-1})	2.8×10^{11}	2.4×10^{11}	2×10^{10} at 80 K	2.9×10^{11}	2.4×10^{11}

Since one of the shortcomings of a QWIP detector is its low quantum efficiency, the use of gratings integrated with each pixel has been developed. The gratings allow the detection of normal-incident light through one of several mechanisms: diffraction,[40] refraction,[41] and total internal reflection.[42] For the case of total internal reflection, a series of angled sidewalls is etched into the superlattice region of a QWIP, as shown in Fig. 11(a). When light is incident from the backside—passing through a thinned substrate—it undergoes total internal reflection off the angled sidewalls. A component of the light is then parallel to the quantum well direction and can be absorbed, as shown in Fig. Fig. 11(b).
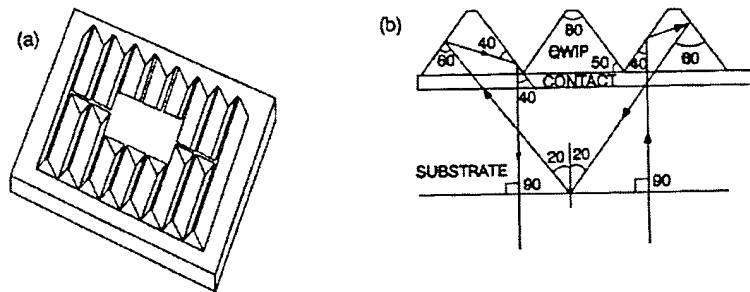
Fig. 11. (a) A profile view and (b) a side view of a series of angled sidewalls etched into the superlattice region of a QWIP. When light is incident from the backside—passing through a thinned substrate—it undergoes total internal reflection off the angled sidewalls.

Using this optical coupling scheme, the ratio of photocurrent to dark current was observed to increase by a factor of 2.4–4.4 and the quantum efficiency and detectivity increased by a factor of 2.4. A grating scheme similar to this one is necessary for FPAs since the large area of the array should be exposed to the maximum photon flux possible, and this occurs when the light is normally incident. Of course, a disadvantage is that it represents an extra processing step in fabricating the FPA.

While a detector sensitive to one region of the infrared is useful for many applications, there is an increasing demand from more rigorous applications for multi-spectral or multi-color detection. Multi-color detection allows for enhanced target discrimination and identification, because the target can now be viewed with improved contrast. An example is illustrated in Fig. 12.
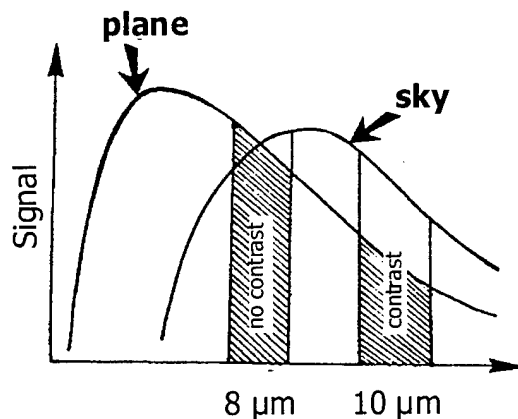

Fig. 12. There is no contrast between the plane and the sky at 8 μm, but at 10 μm the two can be distinguished.

Suppose one were to attempting to seek out an airplane against the backdrop of the sky. The plane and the sky each has its own unique emission spectrum, shown in the figure. Using a detector sensitive at 8 μm, the plane and the sky cannot be distinguished because they both have the same signal at that wavelength, even though their spectra are clearly different. The solution is to have another detector sensitive at a different wavelength, in this case 10 μm, where the signals of the two sources are different. By viewing at both these wavelengths, the plane can be picked up from the sky.

Methods that have been employed include the use of dichroic filters, mechanical filter wheels, or a dithering system with a striped filter on multiple FPAs. These are not satisfactory

because they come with a large cost, size, complexity, and cooling requirements. There are also spatial alignment and temporal registration problems when attempting to synchronize separate FPAs. Having a single, multi-color FPA can do away with these problems.

Of all the cooled infrared detector systems, multi-color FPAs have been demonstrated only for HgCdTe and QWIPs. Just as was true for single-color FPAs, recent results show that the QWIP multi-color FPAs have superior operability than their HgCdTe counterparts. For a HgCdTe MWIR/LWIR FPA, with cutoff wavelengths of 4.67 μm and 8.76 μm, the pixel operability was 95.2% and 93.0% in the MWIR and LWIR, respectively.[43] For a QWIP LWIR/LWIR FPA, the operability was greater than 99% at both 8.6 μm and 11.2 μm.[44]

QWIP FPAs also are not limited to two color detection, as is the case for HgCdTe FPAs. Demonstrations have been made for as many as a four-color QWIP.[45] For this device, the structure contained four superlattices—grown in one step—of GaInAs/AlGaAs for the MWIR (4.7 μm) and GaAs/AlGaAs for the LWIR (8.5 μm, 9.0 μm, and 12.3 μm). This is a feature of using unipolar superlattices, which can effortlessly be stacked upon one another.

To finish this section, a summary of the advantages and disadvantages of HgCdTe detectors and QWIPs is presented in Table 3. While HgCdTe might give better performance for a single detector at temperatures above 70 K, QWIPs are very competitive for FPA operability, especially at low temperatures and in the VLWIR.

Table 3. The advantages and disadvantages of HgCdTe detectors and QWIPs.

Detector type	Advantages	Disadvantages
HgCdTe	• Excellent quantum efficiency • Very high detectivity • Bandgap can be adjusted to vary detection wavelength • Multi-color arrays demonstrated	• Poor array operability and uniformity • Material defects result in low R_0A for many VLWIR pixels, R_0 non-uniform • RAD-hard arrays are difficult due to narrow bandgap and defects in material • HgCdTe material results in low yield and high costs for large-area arrays • Reproducibility is poor due to large sensitivity of bandgap to composition
QWIP	• Mature III-V growth technology • Wide-bandgap material is better for RAD-hard applications. • Excellent array uniformity • High R_0A allows long integration time • VLWIR demonstrated using standard QWIP technology, no unique steps • Multi-color arrays demonstrated	• Lower quantum efficiency than intrinsic HgCdTe • Requires lower sensor temperature than intrinsic detectors for $\lambda < 12$ μm • Normal incidence detection requires additional pixel fabrication steps (etching of micro-gratings)

2.7. Alternatives to GaAs/AlGaAs

Just as HgCdTe is the most popular material system for infrared detectors, GaAs/AlGaAs is the material system of choice for QWIPs, since it historically has been the most studied III-V material system. However, the GaInAs/InP material system possesses several important advantages over GaAs/AlGaAs that could lead to improved QWIP performance.

The first is that GaInAs/InP QWIPs use a binary barrier, InP, while GaAs/AlGaAs QWIPs use a ternary barrier, AlGaAs. Binary layers have an inherently lower defect density than ternary layers, which translates into lower dark current, especially at cryogenic temperatures. The second is that GaInAs is an aluminum-free material. The DX-defect centers associated with

19

Al are avoided, and fabrication of Al-free devices is more straightforward since passivation is not required. The third is that the effective mass of electrons is lower for GaInAs/InP than for GaAs/AlGaAs. The drift mobility and tunneling properties will be better as a result.

The first GaInAs/InP QWIP was fabricated by Gunapala *et al.* in 1991.[5] The structure was grown by MOMBE with 20 periods of 60 Å GaInAs/500 Å InP, with the peak absorption wavelength occurring at 8.1 μm. The responsivity of this device was 6.5 A/W at a bias of 3.5 V, which is a factor of five times larger than similar GaAs/AlGaAs QWIPs. This is directly attributable to the larger gain and hot electron mean free path of the device. At 3.5 V, the gain was 9.0 and the hot electron mean free path was 10 μm, which for both is approximately an order of magnitude larger than comparable GaAs/AlGaAs QWIPs.

3. QWIP performance

3.1. GaAs/GaInP QWIPs (λ = 8–20 μm)

GaAs-GaInP n-type QWIP structures were grown using gas-source molecular beam epitaxy (GSMBE) on (100) semi-insulating GaAs substrates. GaAs well widths were 40Å, 65Å, and 75Å respectively, and the lattice-matched $Ga_{0.51}In_{0.49}P$ barriers were 500Å thick. Each sample superlattice had 20 periods. The silicon doping in the quantum wells was 5 x 10^{17} cm^{-3}.

The photoresponse for three different well widths is shown in Fig. 13. The peak wavelengths of the three samples are 10.4, 12.78, and 13.3 μm for well widths of 40, 67, and 75 Å respectively. The cutoff wavelengths are 13.5 μm, 15, and 15.5 μm for the three samples. The full width at half maximum (FWHM) for the three samples in meV (and as $\Delta\lambda/\lambda$) were 185 meV (0.58), 37 meV (0.5), and 42 meV (0.375) respectively. These FWHM are typical for bound to continuum QWIPs. The reduction in FWHM for wider wells indicates that the second excited state in these samples is closer to resonance with the barrier energy.
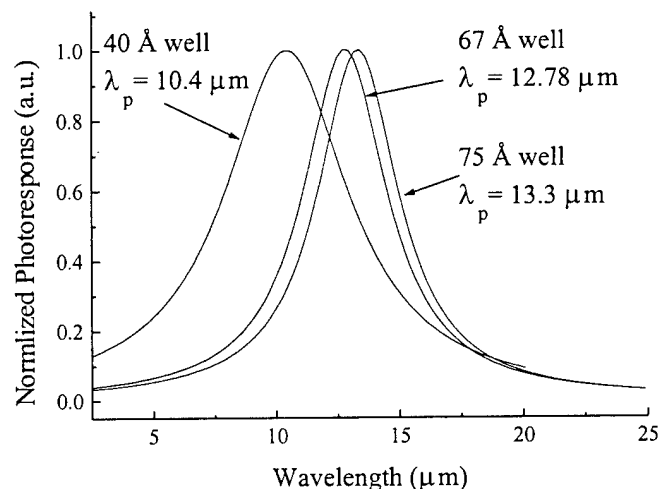

Fig. 13. Normalized optical response at 77K for samples with 40Å, 65Å and 75Å quantum wells.

Shown in Fig. 14 is the calculated absorption coefficient for a 75Å well GaAs/GaInP QWIP. The calculated peak absorption of 12.9 μm and an approximately 14 μm cutoff wavelength agree very well with the observed photoresponse shape.
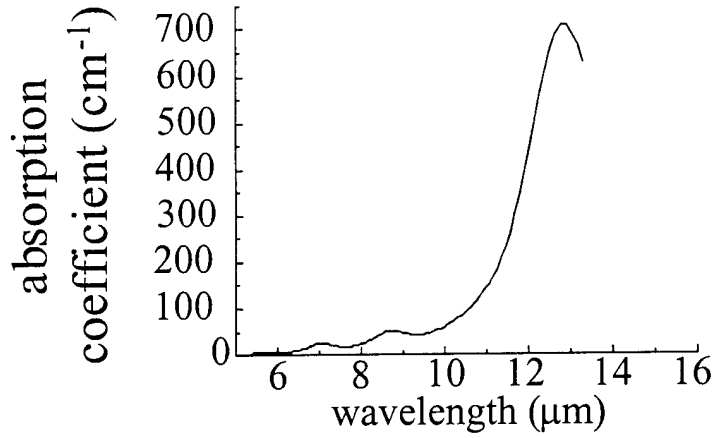
Fig. 14. Calculated absorption spectrum for 75Å GaAs / 500Å GaInP superlattice.

Fig. 15 shows the typical dark currents measured at different temperatures. The observed asymmetry with bias may be due to an asymmetric quantum well profile or doping impurity segregation.
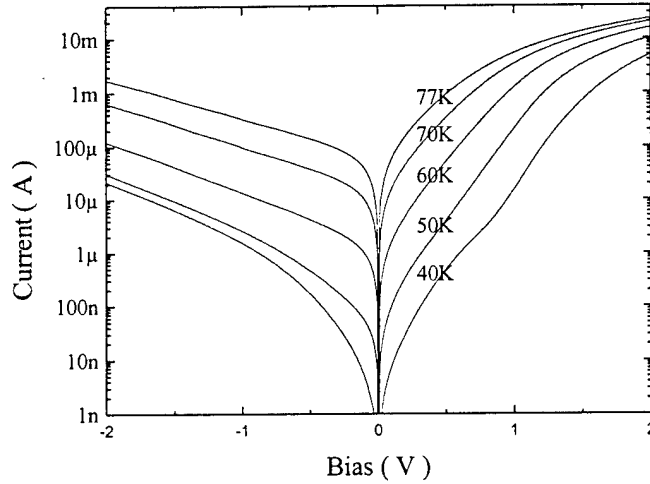

Fig. 15. Measured QWIP dark current from 30 to 77 K for the sample with 65 Å quantum wells.

At low bias, where tunneling can be neglected, the dark current I is expected to increase exponentially with temperature following Eq. 12:

$$I \propto T \exp\left(-\frac{\Delta E}{kT}\right) \qquad (12)$$

Therefore, the activation energy can be obtained by calculating the slope of log (I/T) versus 1/kT. For the three samples with 40Å, 65Å, and 75Å wells, the activation energies ΔE are 37, 50, and 46 meV respectively.

The quantum well subband energies were determined using a four-band Kane model, which includes the effects of band non-parabolicity and band mixing. The electron-electron

21

exchange interaction effect was also included, and the depolarization and excition shifts were neglected as before.

From these subband energy levels and the dark current activation energies we computed the conduction band offset ΔE_c to be 121.1 meV $\pm$ 2 meV. A summary of the data used in this model is given in Table 4. From the known bad gaps of GaAs and GaInP, the band-gap difference ΔE_g = 483 meV is obtained.[46] Using our experimentally determined conduction band offset, a band ratio offset ratio of $\Delta E_c/\Delta E_g$ = 0.251 is calculated, which matches the assumed ratio used for theoretical modelling. Values of ΔE_c in the literature range between 80 to 240 meV. However, the only previous measurement for material grown by GSMBE was 108 meV.[47] This experimental result agrees well with these previous results.

Table 4. The conduction band offset is calculated as $\Delta E_C = (E_O - E_{EXCH}) + E_F + \Delta E$, where E_O is the ground state energy, E_{EXCH} is the electron-electron interaction energy, E_F is the Fermi energy, and ΔE is the activation energy.

Well (Å)	$E_0 - E_{EXCH}$	ΔE	E_F	ΔE_c
40	79	37	4.4	120.4
65	62	50	10.4	122.4
75	59	46	12.5	120.5

The dark current density (A/cm^2) at 77K for sample B as a function of electric field (V/cm) is shown in Fig. 16. The results of Levine[7] for a GaAs/AlGaAs QWIP with similar well doping density, and cutoff wavelength is shown for comparison. The smaller dark current may be due to GaAs/Ga$_x$In$_{1-x}$P's larger mobility,[48] smaller surface recombination velocity,[49] or smaller interface roughness,[50] by comparison to GaAs/Al$_x$Ga$_{1-x}$As.
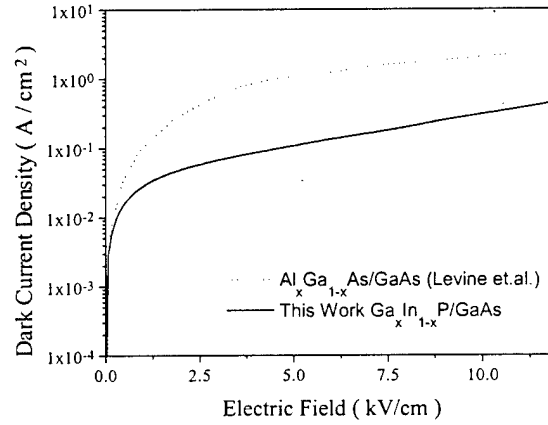

Fig. 16. Measured dark current density for sample C compared to GaAs/AlGaAs results in Ref. 7.

We have modeled the dark current by assuming thermodynamic carrier equilibrium and a drift model[51] where the drift velocity is proportional to the electric field according to:

$$v_d = \frac{\mu V}{L_b}\left[1+\left(\frac{\mu V}{v_s L_p}\right)^2\right]^{-1/2} \tag{13}$$

22

where μ is the mobility, V is the applied bias per quantum well, and L_p is the period thickness. We have neglected any complications to do with the way in which carriers in the quantum well are replenished and the mechanisms of charge transfer from the emitter contact to the MQW. Since the carriers which are thermally excited into the continuum transport states and contribute to the dark current are originally from the quantum wells, a 2-D density of states (DOS) is used, and the effective number of carriers contributing to the current is then given by Eq. 8.

In calculating the transmission coefficient T(E,V) we have used T(E,V)=1 for E larger than the conduction band offset V_o and the Wentzel-Kramers-Brillouin (WKB) approximation[52] for E < V_o. In the calculation we take the conduction band offset V_o to be 0.1 eV.[53] Conduction band non-parabolicity is neglected because it has been shown to have a negligible effect on dark current,[51] but image charge effects have been included.

The dark current measurements for sample B are shown in Fig. 17 as function of voltage and temperature and compared with the calculated values. Good agreement is achieved as a function of both bias and temperature over seven orders of magnitude in dark current. These calculations use a drift mobility of 1000 $cm^2V^{-1}s^{-1}$, a saturation velocity of 1.5 x 10^5 cm^{-1} and the nominal sample parameters shown in Table 4. The saturation velocity is approximately one order of magnitude lower than typical values for bulk GaInP at 77K[54,55] in a similar electric field, as would be expected because of re-trapping by quantum wells and interface scattering.
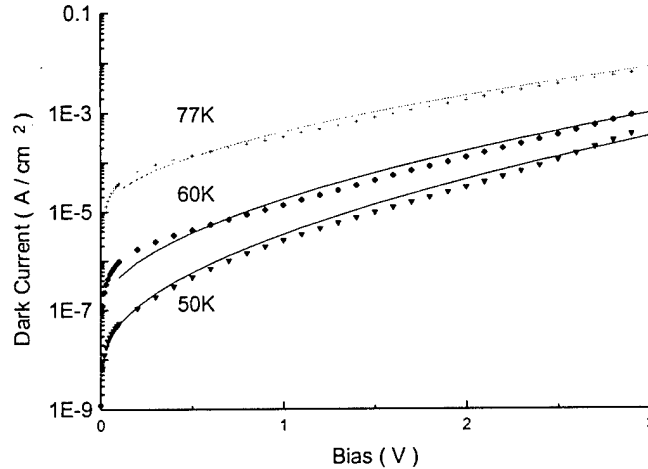

Fig. 17. Comparison of experimental (points) and theoretical (lines) dark current-voltage curves at various temperatures for sample B.

The photoconductive gain is ratio of the distance traveled by an electron before recapture l to the thickness of the device L. At the biases used in this experiment, $l = v_d(E)\cdot\tau$ and therefore

$$g = v_d(E)\cdot\tau / L. \tag{14}$$

In order to evaluate the carrier lifetimes in these GaAs/GaInP detectors, we have directly measured the noise current as a function of bias using a spectrum analyzer at $T = 77K$. This noise is dominated by generation-recombination noise at $T = 77K$. From the equation for G-R noise given by Eq. 9, we calculate the gain using the dark current-bias data from Fig. 17, and then calculate the carrier lifetimes using Eq. 14. Fig. 18 shows the carrier lifetimes and gain derived from noise measurements for sample B.
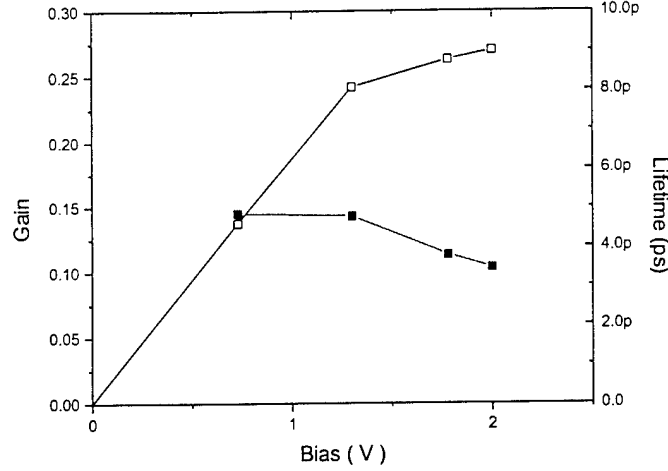
23

Fig. 18. Calculated gain and recombination lifetimes as a function of applied bias for sample B.

3.2. GaInAs/InP QWIPs (λ = 8–9 μm)

Parameters such as well doping profile, well doping density, number of periods, and barrier thickness each play a role in QWIP performance and the optimized values must be found for each. All growths in this section were done by LP-MOCVD on semi-insulating InP substrate. The LWIR measurements were taken at 80 K with normal incidence. No polishing or faceting was done, neither was any kind of surface grating applied. Useful comparisons are drawn between the results of the devices to determine the optimized values of the device parameters.

The dark-current-limited specific detectivity of a QWIP is expressed as[56]

$$D^* = \frac{\lambda \eta}{2hc\sqrt{N}} \sqrt{\frac{\tau_L}{N_{2D}}}, \tag{15}$$

where η is the quantum efficiency, h is Planck's constant, c is the velocity of light, N is the number of quantum wells in the QWIP, τ_L is the carrier lifetime, and N_{2D} is the two-dimensional well sheet carrier density, given by

$$N_{2D} = \frac{m^* kT}{\pi \hbar^2} \exp\left(-\frac{hc}{\lambda_c kT} + \frac{E_F}{kT}\right), \tag{16}$$

where m^* is the electron effective mass in the well, $\hbar$ is the reduced Planck's constant, k is Boltzmann's constant, T is temperature, λ_c is the detector cutoff wavelength, and E_F is the quantum well Fermi level. Thus to increase the specific detectivity, one must increase the quantum efficiency and/or the carrier lifetime of the QWIP. Moreover, the specific detectivity can be expressed in terms of the Fermi level as[57]

$$D^* \propto E_F \exp\left(-\frac{E_F}{2kT}\right), \tag{17}$$

24

which has a maximum value when $E_F = 2kT$. When $T = 80$ K, the optimal value of E_F is 13.8 meV.

While GaInAs/InP QWIPs have been grown by MOMBE,[5] LP-MOCVD,[6] and GSMBE,[58] little work has been completed to optimize the performance of GaInAs/InP QWIPs. In this section, we report the influence of the GaInAs quantum well doping density on responsivity, dark current, noise current, and detectivity for GaInAs/InP QWIPs ($\lambda = 9$ μm) grown by LP-MOCVD.

All epitaxy for this study took place inside an LP-MOCVD reactor.[59] Triethylgallium and trimethylindium are the group III sources, arsine and phosphine are the group V sources, and silane is the n-type dopant. The growth temperature was 480°C and the growth pressure was 78 torr. First, we performed the optimization of the crystal growth of InP and GaInAs. The quality of the epilayers was assessed by high-resolution x-ray diffraction, scanning electron microscopy, photoluminescence, and Hall mobility. The doping density for a bulk epilayer was measured with electrochemical capacitance voltage characterization which we then applied for doping the quantum wells.

Second, we grew three series of GaInAs/InP QWIPs with three different quantum well doping densities whose structures contained 20 quantum wells of 60 Å-thick n-GaInAs surrounded by 500 Å-thick undoped InP barriers on semi-insulating InP substrate; these structures are designed for detection in the $\lambda = 8$–9 μm range. On each side of the well region are a 0.50 μm-thick top and a 0.75 μm-thick bottom n-GaInAs contact layers doped to 1×10^{18} cm^{-3}. The outermost 5 Å of each quantum well were undoped to prevent impurity diffusion into the barrier. The quantum well doping densities used are 1.7×10^{17} cm^{-3} (Series A), 5×10^{17} cm^{-3} (Series B) and 1.7×10^{18} cm^{-3} (Series C). A schematic diagram of the QWIP structure is shown in Fig. 19.

Ti/Pt/Au contacts

0.50 μm InP n+ top contact layer
} 20 period n-GaInAs/InP SL
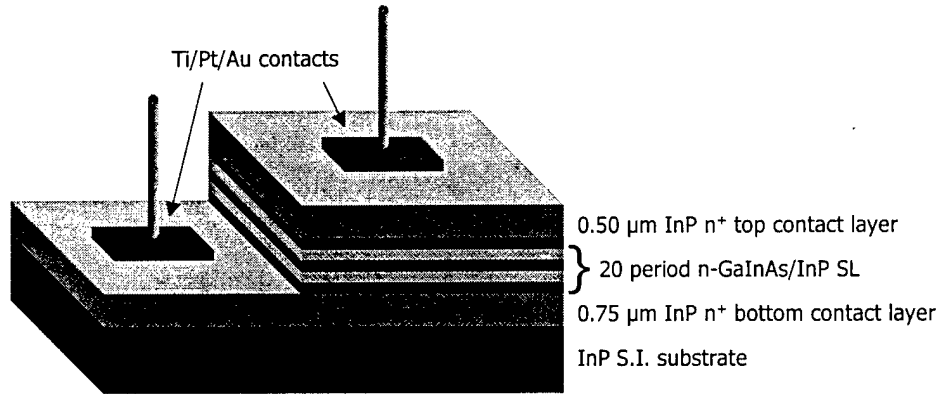0.75 μm InP n+ bottom contact layer
InP S.I. substrate

Fig. 19. A schematic diagram of the GaInAs/InP QWIP on InP substrate. This is how the device appears after fabrication, with the mesas etched and the metal contacts deposited.

After epitaxy, 400×400 μm mesas were patterned with an electron cyclotron resonance-enhanced reactive ion etch reactor using a $BCl_3/Cl_2/Ar$ etch chemistry that yielded approximately 45° sidewalls and then Ti/Pt/Au metal contacts were deposited with electron-beam evaporation. The device measurements took place at a temperature of 80 K inside a liquid nitrogen cryostat with normal incidence illumination. The angled mesa sidewalls serve to couple the incident light parallel to the quantum wells and allow for normal incident illumination.

The dark current for the three GaInAs/InP QWIP series at $T = 80$ K is reproduced in Fig. 20. The noise currents are 8.0×10^{-14} AHz$^{-1/2}$, 1.0×10^{-13} AHz$^{-1/2}$, and 1.3×10^{-11} AHz$^{-1/2}$ at a

bias of 1 V for Series A, B, and C, respectively. This trend in the both the dark and noise current is due to a substantial increase in the Fermi level with doping, which in turn causes a decrease in the activation energy. For Series A, B, and C, the calculated Fermi levels are 1.7 meV, 16.3 meV, and 56.6 meV, respectively, above the first bound state. A detailed description of Fermi level calculation is given elsewhere.[60] The relative spectral response for the three series is shown in the inset of Fig. 21. Given that each of the three series has the same peak spectral response at $\lambda = 9.0$ µm, and hence the same first bound level energy, then the large increase in the Fermi level is responsible for the drop in the activation energy.
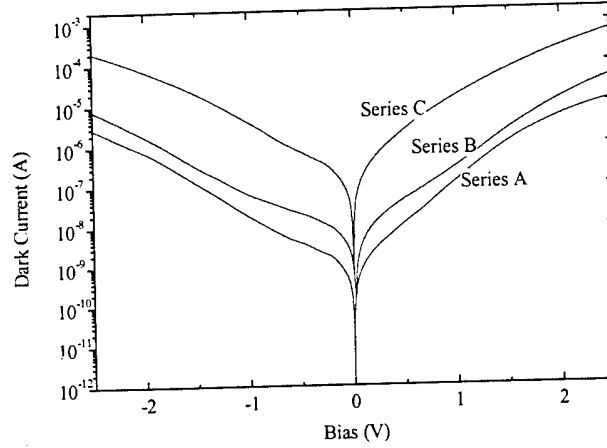

Fig. 20. The dark current as a function of bias of the three GaInAs/InP QWIP series.

To analyze the trend in dark current, we can model the dark current as $I_D = n^* qvA$, where v is the average drift velocity, A is the device area, and the effective number of electrons thermally excited out of the well n^* is[61]

$$n^* = \frac{m^* kT}{\pi \hbar^2 L_p} \exp\left(-\frac{\Delta E_c - E_1 - E_F}{kT} \right),$$ (18)

where L_p is the period thickness, ΔE_c is the conduction band offset, and E_1 is the energy of the first bound level. We therefore expect the ratio of dark current to equal the ratio of thermally excited carriers from Eq. 18. Between Series B and A, the calculated dark current ratio is 3.2, while between Series C and B the calculated dark current ratio is 44. This is in good agreement with the actual dark current ratios: between Series B and A the dark current ratio is 3.5, while between Series C and B the ratio is 61. Over a larger than two order of magnitude change in dark current, the fit is within 30%.

Also, we fabricated two additional QWIPs identical to Series A but with 750 Å- and 1000 Å-thick InP barriers, and discovered no significant change in dark current amongst the these three QWIPs as a function of applied electric field. So there is no advantage to using thicker barriers in an effort to reduce the dark current.

The graph of responsivity for the three GaInAs/InP QWIP series is pictured in Fig. 21. For the case of Series B at a bias of 5 V, the responsivity is 33.2 AW^{-1}, which is to the authors' knowledge the largest absolute responsivity and the largest ratio of responsivity to electric field for QWIPs in this wavelength range ($\lambda = 8$–9 µm). From the Fermi levels given above we can

determine the concentration of ionized carriers within each series which are able to contribute to photocurrent and hence the responsivity.[62] Between Series B and A, the ratio of ionized carriers is 7.0, which closely matches the measured responsivity ratio of 7.6. The sharp drop in Series A is most likely is due to the depletion of carriers inside the well because the doping density is critically low. Between Series C and B, the ratio of ionized carriers is 3.7, somewhat higher than the measured responsivity ratio of 2.2 between the two series.
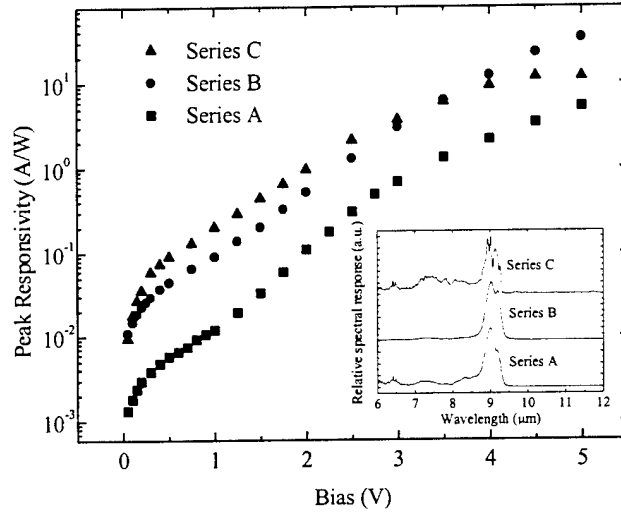

Fig. 21. The peak responsivity as a function of bias of the three GaInAs/InP QWIP series. The inset shows the relative spectral response of the three QWIP series.

The detectivity of the three GaInAs/InP QWIP series is calculated and plotted in Fig. 22. Since the detectivity is proportional to the responsivity divided by the current noise, Series A's detectivity is lower because its responsivity was much lower than the other two series while Series C's detectivity is lower because its current noise was much higher than the other two series. Series B has the optimal quantum well doping density to avoid these two pitfalls, and yields a maximum detectivity of 3.5×10^{10} cmHz$^{1/2}$/W at a bias of 0.75 V. In addition, the Fermi level of 16.3 meV for Series B is in excellent agreement with Eq. 17 which states that the optimal Fermi level is 13.8 meV.
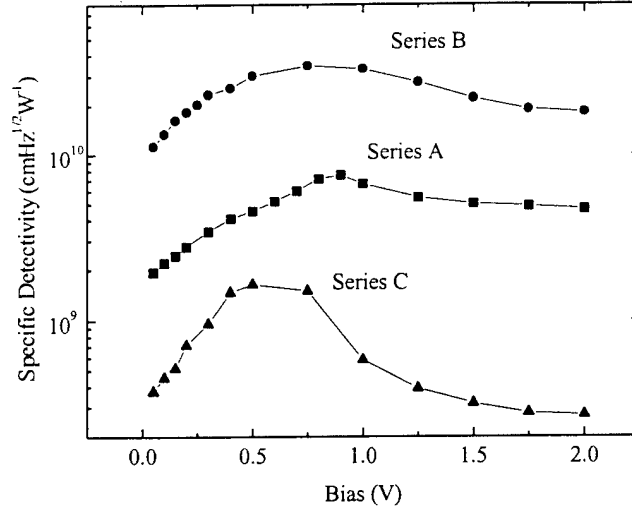
Fig. 22. The specific detectivity as a function of bias of the three GaInAs/InP QWIP series.

The detectivity amongst the three series is very sensitive to doping. By changing the quantum well doping density by a factor of 10, the detectivity changes by over a factor of 20. Thus it is extremely crucial to fabricate GaInAs/InP QWIPs with the optimal quantum well doping density. This is in stark contrast to GaAs/AlGaAs QWIPs, where changing the quantum well doping density by over a factor of 30 changed the detectivity by only a factor of two.[62]

The much larger sensitivity of detectivity to doping in GaInAs/InP QWIPs versus that of GaAs/AlGaAs QWIPs can be explained by Eq. 17. The relationship between the Fermi level and ionized carrier density N_D can be approximated by $N_D \approx m^* E_F / \pi \hbar^2 L_w$, where L_w is the quantum well thickness. Solving for E_F yields $E_F \approx N_D \pi \hbar^2 L_w / m^*$. The Fermi level scales with the ionized carrier density as L_w/m^*. The larger the factor L_w/m^* is, the sharper the peak of detectivity as a function of ionized carrier density according to Eq. 17. In other words, the larger the factor L_w/m^* is, the larger the sensitivity of detectivity to the ionized carrier density. For GaInAs/InP QWIPs, both the well width is larger (60 Å v. 40 Å) and the well effective mass is smaller ($0.041m_0$ v. $0.067m_0$) than for the GaAs/AlGaAs QWIPs in Ref. 62. Thus the factor L_w/m^* will be significantly larger, and the sensitivity of detectivity to the doping density will also be larger. This partly explains the observed difference of the sensitivity of detectivity between the two material systems.

Another difference may be the dependence of carrier lifetime on doping density. Gain values calculated from noise measurements for these samples are 0.40, 1.0, and 10 for Series A, B, and C, respectively, at 1 V bias. Assuming the transit time is approximately the same for QWIPs fabricated from either GaInAs/InP or GaAs/AlGaAs at equal electric fields, the measured gain values are proportional to the carrier lifetime.[63] The values of gain measured here for GaInAs/InP QWIPs vary more strongly (by over one order of magnitude) with quantum well doping density than values measured for the GaAs/AlGaAs QWIPs in Ref. 62 (by a factor of two) for the same range of doping density, and therefore also contribute to the sensitivity of detectivity with doping.

3.3. AlGaInAs/InP and GaInAs/AlInAs QWIPs (λ = 3–20 μm)

In this section, we demonstrate that high quality quantum well infrared photodetectors in both the 3-5 μm and 8-20 μm spectral bands can be grown on InP substrate using gas-source molecular beam epitaxy.

The device parameters of the QWIPs studied are listed in Table 5, where L_B represents the barrier width, L_W is the well width, and N_D denotes the donor doping concentration of the quantum wells. The wafers were grown using an EPI modular Gen-II gas-source molecular beam epitaxy system equipped with arsine and phosphine sources for As and P. Metallic gallium and indium were used for group III elements. The devices were grown on semi-insulating InP (100) substrates. After epitaxial growth, standard photolithographic process is used to fabricate mesa photodetectors. A square active area of 1.6×10^{-3} cm^2 was defined and 1600 Å-thick AuGe/Ni/Au ohmic contacts were deposited by electron beam evaporation and patterned using a lift-off process.

Table 5. Device parameters for the measured QWIPs.

QWIP	B	A	C	D
Barrier material	$Al_{0.48}In_{0.52}As$	InP	InP	InP
L_B	500 Å	500 Å	500 Å	500 Å
Well material	$In_{0.53}Ga_{0.47}As$	$In_{0.53}Ga_{0.47}As$	$In_{0.52}Ga_{0.38}Al_{0.1}As$	$In_{0.52}Ga_{0.33}Al_{0.15}As$
L_W	35	56	60	65
N_D	2×10^{18} cm^{-3}	5×10^{17} cm^{-3}	5×10^{17} cm^{-3}	5×10^{17} cm^{-3}
Periods	25	20	25	25

3.3.1. GaInAs/InP QWIPs

The spectral response of QWIP-A at 80K is measured by using a Mattson Fourier transform IR spectrometer (GL3020). Absolute responsivity is measured using a Mikron blackbody source (M305) chopped at 500Hz and an EG&G 5209 lock-in amplifier. The blackbody temperature was 800K. Peak responsivity was calculated by integrating the normalized spectral response with the blackbody responsivity. The normalized spectrum under an applied electric field of 10 kV/cm is shown in Fig. 23. The photoresponse peak is found to be 8.1 μm and the cutoff wavelength is about 9 μm.
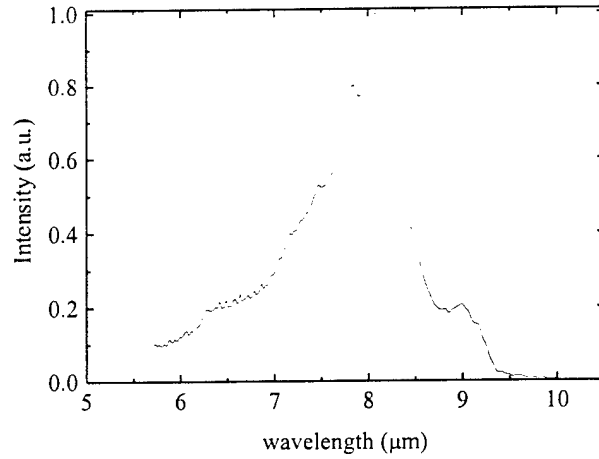
Fig. 23. Normalized spectral response at 80K with a peak of 8.1 μm.

The peak responsivity value of 7.5 A/W at 5 V reverse bias (not pictured) is approximately one order of magnitude higher than that typically obtained in AlGaAs/GaAs QWIPs. The specific detectivity (D*) and noise current of the QWIP at 80K are shown as a function of applied electric field in Fig. 24. The maximum D* of the QWIPs measured in this work was found to be 5×10^{10} cm √Hz / W at 1.2 V.
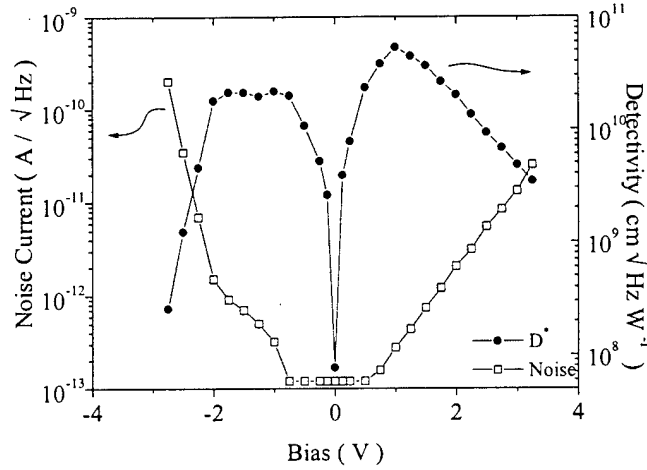

Fig. 24. Detectivity and noise current for InGaAs/InP QWIP as function of bias.

3.3.2. GaInAs/AlInAs QWIPs

In order to determine the wavelength range at which InGaAs/InAlAs QWIPs can operate, we have calculated the energy levels in InGaAs/AlInAs MQW structures. For this calculation, we have assumed $m_{well} = 0.041 \cdot m_o$, $m_{barrier} = 0.075 \cdot m_o$, $Eg_{77Kwell} = 1.508$ eV, $Eg_{77Kbarrier} = 0.801$, and $\Delta Ec = 0.5$ meV. In Fig. 25 the n=1 and n=2 electron energy levels are plotted versus the well width. The n=2 level is confined to the well for well widths larger than 35 Å, and is an extended band for narrower wells. For wells thicker than 35 Å the intersubband absorption energy is plotted as an dashed line calculated from the energy difference between the n=1 and n=2 states. For narrower wells the absorption energy is plotted as a dotted line calculated from the difference in energy between the confined n=1 and the center of the continuum band. The

30

experimental data points for samples with quantum well widths of 30 Å, 35 Å, and 40 Å are also shown, demonstrating good agreement with our model calculations.
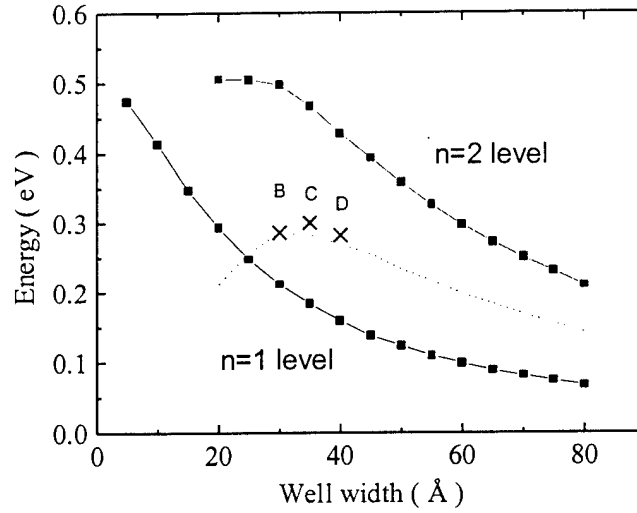

Fig. 25. The calculated two first electron levels in InGaAs/AlInAs quantum wells (solid lines) vs. well width. Experimental data points obtained for samples with well widths of 30 Å, 35 Å, and 40 Å are shown as well.

The relative spectral response for the three samples was measured using a Mattson Fourier transform infrared (FTIR) spectrometer. The measurements were made at T=77K under varying forward and reverse biases. No change in the shape of the spectral response occurred for ±5 V bias for these samples.

The result of the measurement is shown in Fig. 26. All three samples have significantly narrower spectrum than previously reported for $In_{0.2}Ga_{0.8}As/Al_{0.38}Ga_{0.62}As$.[8] The difference in spectral width when the well is changed from L_w = 30 Å to 40 Å is in excellent agreement with our theoretical calculations. According to the calculations, the first excited state for the 30 Å sample is in the continuum, resulting in a broad absorption spectrum. On the other hand, the excited state in the 35 Å sample is just slightly bound (quasi-bound), and in the 40 Å sample is more strongly bound. In either case, the intersubband absorption for both is narrow in excellent agreement with experiment. To our knowledge, the spectral width (Δv = 0.13 µm) of the 40 Å well sample is the narrowest reported for a QWIP.
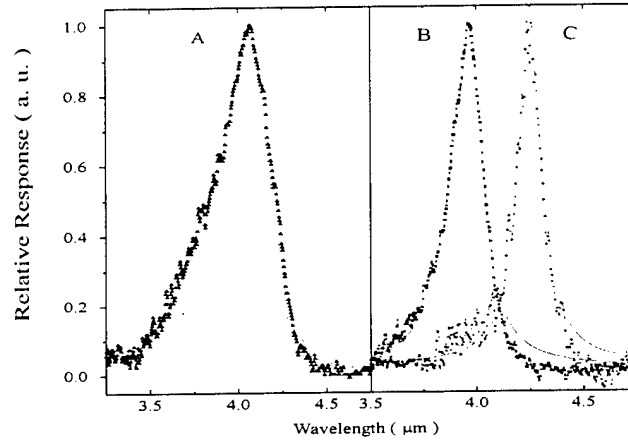
Fig. 26. Measured spectral responsivity of samples A-C at T=77K with 1 V reverse bias.

3.3.3. AlGaInAs/InP QWIPs

The bandgap of InGaAlAs can be engineered between the two boundary ternary alloys, $In_{0.53}Ga_{0.47}As$ (0.76 eV) and $In_{0.52}Al_{0.48}As$ (1.46 eV). The growth of InGaAlAs alloy is relatively easier than InGaAsP due to the following reasons:[64] (1) only one group V element (As) is incorporated, avoiding the problem of As/P ratio control; (2) composition of the layer is controlled by each constituent element's flux intensity; and (3) near-unity sticking coefficients of the three group III elements facilitate reproducibility of composition.

For these experiments, three structures were grown by gas-source molecular beam epitaxy with arsine and phosphine as group V sources, elemental gallium and indium as group III sources, and elemental silicon as an n-type dopant source. The AlAs mole fraction in $In_{0.52}(Ga_{1-x}Al_x)_{0.47}As$ and the quantum well width for the three samples were (x=0, 56 Å), (x=0.1, 60 Å), and (x=0.15, 65 Å) respectively, as listed in Table 6. Each structure consisted of twenty periods of InGaAlAs quantum wells separated by 400 Å InP barriers. The quantum wells were doped n=8x10^{17} cm^{-3}. Top and bottom 0.6 µm layers of n=1x10^{18} cm^{-3} $In_{0.53}Ga_{0.47}As$ were grown for ohmic contacts.

Table 6. The AlAs mole fraction in $In_{0.52}(Ga_{1-x}Al_x)_{0.47}As$ and the quantum well width for the three samples studied.

Sample	Composition	Quantum well width
A	$In_{0.53}Ga_{0.47}As$	56 Å
B	$In_{0.52}Ga_{0.38}Al_{0.1}As$	59 Å
C	$In_{0.52}Ga_{0.33}Al_{0.15}As$	66 Å

The responsivity spectrum of the three samples measured at T = 10K are shown in Fig. 27. For a bias of -1 V (mesa top negative), the 50% long wavelength cutoff wavelengths for the three samples were 8.5, 13.3, and 19.4 µm, respectively. The peak and cutoff wavelengths, and linewidth $\Delta\lambda/\lambda$ for the three samples are given in Table 7.
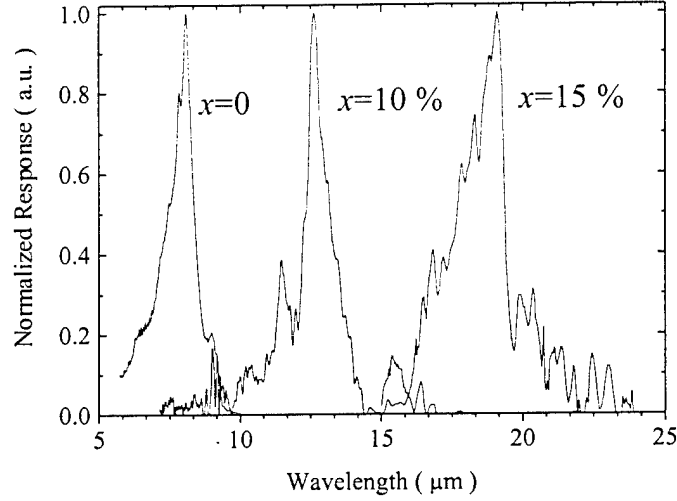
Fig. 27. Normalized spectral response for $In_{0.52}(Ga_{1-x}Al_x)_{0.48}As/InP$ QWIPs with $x=0$, $x=0.1$, and x-0.15 mole fraction of AlAs.

Table 7. Spectral response parameters for the three samples studied.

Sample	Peak wavelength (μm)	Cutoff wavelength (μm)	FWHM ($\Delta\lambda/\lambda$)
A	8.1	8.5	12.5 %
B	12.7	13.3	8%
C	19	19.5	9%

The absolute responsivities were measured by using a calibrated blackbody source. The detectors were back illuminated through a 45° polished facet. The bias dependence of the responsivity was measured for samples A and B at $T=77K$ and the results are shown in Fig. 28 for both positive and negative bias. The responsivity of sample C was too low to be measured at $T=77K$. The peak responsivity at -1 V of the $In_{0.52}Ga_{0.38}Al_{0.1}As/InP$ QWIP (sample B) was 0.37 A/W. This is comparable (20 % higher) to the InGaAsP/InP QWIP (1.3 μm bandgap, $L_W=63$ Å) reported by Gunapala et al.[65] which had a similar 13.2 μm cutoff wavelength. It is worth noting the responsivity for these samples are approximately five times as large as the best responsivity measured for GaAs/AlGaAs QWIPs.
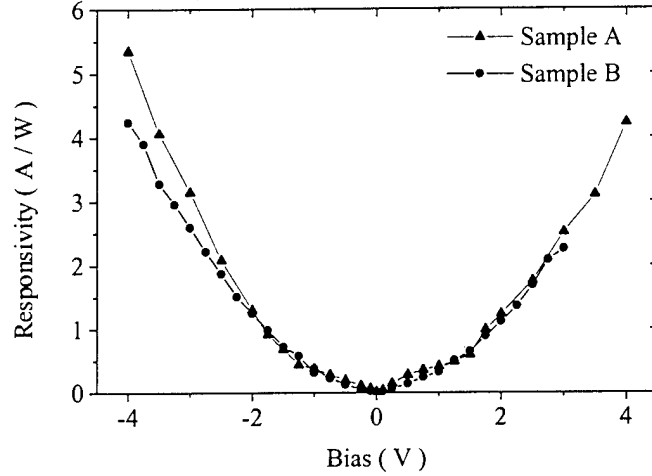
33

Fig. 28. Bias dependence of peak responsivity measured at T=77K for InGaAs/InP (sample A) and $In_{0.52}Ga_{0.38}Al_{0.1}As/InP$ (sample B) QWIPs.

The noise current i_n, of the $In_{0.52}Ga_{0.38}Al_{0.1}As/InP$ and $In_{0.53}Ga_{0.47}As/InP$ QWIPs were measured at T=77K as a function of bias voltage using a spectrum analyzer and found to be i_n=80– and 0.4-pA at bias voltages of V_B= -1 V. The peak detectivities, $D*_\lambda$ can now be calculated from $D^*_\lambda = R\sqrt{A\Delta f}/i_n$ where A=1.6×10^{-4} cm^2 is the device area and Δf=1 Hz is the bandwidth. At an operating bias of V_B= -1 V and T=77K the measured values for the $In_{0.52}Ga_{0.38}Al_{0.1}As/InP$ QWIP are R_P=0.37 A/W, i_n= 80 pA/√Hz and thus D*=1×10^9 cm √Hz W^{-1}. The detectivity of the first sample (GaInAs/InP QWIP) at T=77K and V_B= -1 V is D* = 4×10^{10} cm √Hz W^{-1}.

Using the spectral response data obtained for these samples, it is possible to estimate the conduction band offset for the $In_xGa_{1-x-y}Al_yAs/InP$ heterojunction. The cutoff wavelength for samples A, B, and C correspond approximately to the energy separation ΔE=E_2-E_1 for the three aluminum compositions, y=0 (A), y=0.1 (B), and y=0.15 (C). The energies of the first and second allowed states for these InGaAlAs-InP samples can be calculated for several possible conduction band offsets using the well widths given in Table 6. The E_g of $In_{0.52}(Ga_{1-x}Al_x)_{0.48}As$ layers was reported by Fujii et al.,[66] and changes linearly from 0.75 eV to 1.47 eV with increasing x. The electron effective mass of $In_{0.52}(Ga_{1-x}Al_x)_{0.48}As$ layers was reported by Olego et al.,[67] and changes linearly from 0.041m_0 to 0.075 m_0 with increasing x. In Table 8, the conduction band offset that best fits the cutoff wavelength observed in Fig. 27 is listed.

Table 8. Conduction band offset and band offset ratio calculated for samples A, B, and C.

Sample	Composition	Well width (Å)	Conduction band offset, ΔE_c	Offset ratio $\Delta E_c/E_G$
A	$In_{0.53}Ga_{0.47}As$	56	229 meV	0.37
B	$In_{0.52}Ga_{0.38}Al_{0.1}As$	59	146 meV	0.29
C	$In_{0.52}Ga_{0.38}Al_{0.15}As$	66	103 meV	0.235

A plot of the fit conduction band offset as a function of aluminum fraction is shown in Fig. 29. The data from samples A, B, and C are indicated on the figure. The line is the band offset predicted by the Harrison model as applied by Ishikawa et al.[68,69]
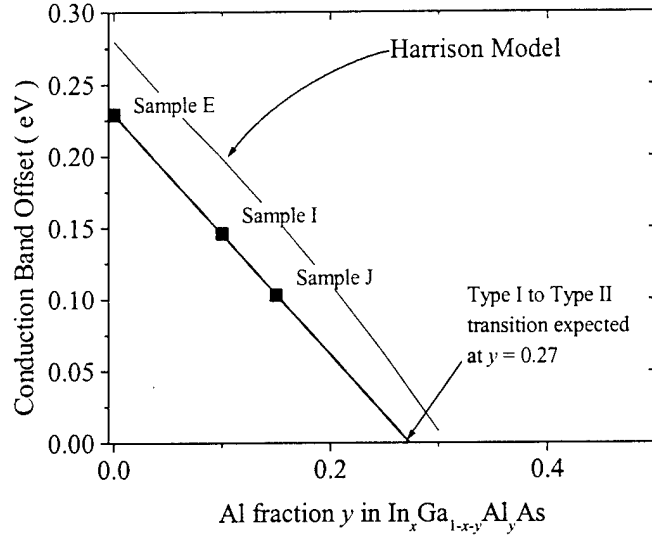
Fig. 29. Conduction band offset values calculated from samples A (0%), B (10%), and C (15%) as a function of Al fraction y in $In_xGa_{1-x-y}Al_yAs$. Also shown is a theoretically derived curve by Ishikawa *et al.* [Ref. 68]

From the experimental data for these QWIPs, it would be expected that the transition from type I quantum well to type II staggered quantum well for $In_{0.53}(Ga_xAl_{1-x})_{0.47}As/InP$ heterojunctions would occur at $y=0.27$. This is less the value ($y=0.33$) predicted by the experimental model, which is based on an interpolation from binary data for InAs, GaAs, and AlAs, but larger than other recent experimental results for GSMBE-grown material: $y=0.18$ calculated from interband absorption by Kawamura *et al.*,[70] and $y=0.23$ calculated from Shottky diode dark currents by Chua *et al.*[64] Because intersubband absorption is very sensitive to the conduction band offset, the measurements presented here represent an accurate method for determining this type I-to-type II transition composition.

3.3.4. Analysis

In order to determine quantitative information about the transport properties of typical QWIP devices, the current and resistance were measured at $T=80K$ as a function of applied voltage using an HP 4155A semiconductor parameter analyzer with the detectors shielded (i.e. dark). The current-voltage curve for QWIP-A is shown in Fig. 30.
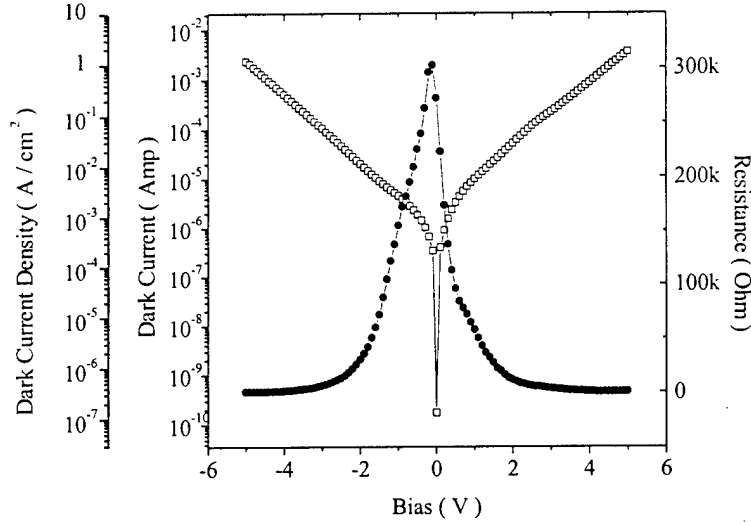
Fig. 30. The dark current and differential resistance vs. applied bias for QWIP-A at T=80K.

The activation energy, E_A, has been calculated from the slope of ln (Idark/T) versus 1/T. The result is shown in Figure Fig. 31. An activation energy of 138 meV is obtained for temperatures above 80K. The expected cutoff wavelength calculated from this energy, λ_C=1.24/0.138 = 8.9 μm, agrees well with the cutoff wavelength of 8.5 μm shown in Fig. 27.
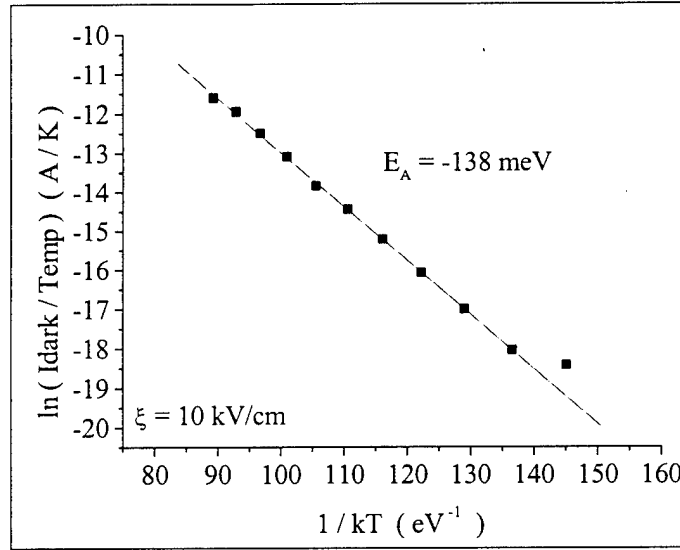

Fig. 31. Activation Energy for thermal dark current.

To determine the gain g, dc or noise measurements can be employed. The dc method requires a measurement of the absorbed photon flux. This measurement is complicated since a fraction of the incoming light is reflected and absolute power levels are difficult to measure accurately. Noise measurements provide an elegant alternative.

Two regions in Fig. 32 are apparent. Near zero bias, the current noise is only weakly dependant on applied bias. In this region, the magnitude of the noise asymptotically approaches the Johnson noise value. At moderate voltages, the noise current begins to increase with increasing applied bias. This increase occurs when the generation-recombination noise current

36

exceeds the thermal noise current. The critical bias V_c where the noise current becomes bias dependent is given by:[71]

$$V_C = \frac{k_B T}{eL_D} \cdot L_{DEVICE} \qquad (19)$$

where L_D is the distance traveled by an excited-state electron before it is recaptured by into a quantum well, and L_{DEVICE} is the total device length (which equals $(L_W + L_B) \cdot N$, where N is the number of periods in the MQW). Although it is difficult to exactly determine V_C from Fig. 32, it is possible to infer $V_C \approx 0.2\text{-}0.3$ V for both samples. At this bias, the noise current is 2X larger than the Johnson noise. This results in $L_D \approx 350 \text{ - } 400$ Å for both samples. Thus, for bias voltages less than V_C, most excited state electrons are recaptured in the same well they were excited from. This determinism results in an external photocurrent noise dominated by thermal fluctuations. When the critical bias is exceeded, excited electrons transport to the next-nearest neighbor well or farther, and the photocurrent noise due to random fluctuations in the trapping and de-trapping rates of electrons grows rapidly.
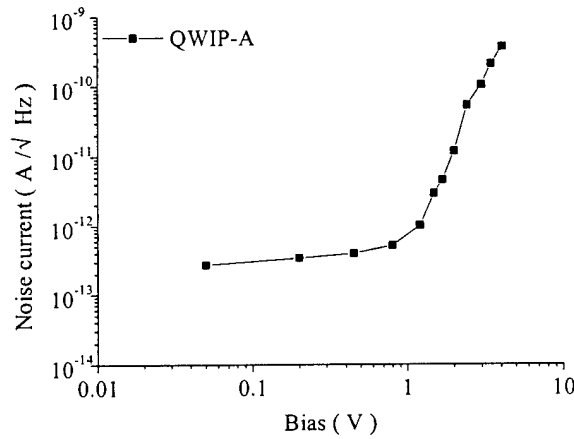

Fig. 32. Noise measurements for InGaAs/InP QWIP at T=77K as a function of bias.

The spectral density of the dark current noise associated with the generation-recombination and trapping of carriers in a photoconductor is written as:[71]

$$S_{idark} = 4e \, I_{dark} \, g_{noise} \qquad (20)$$

where g_{noise} is the noise gain. It has been shown[72] that $g_{noise} = g_{photo}$. Accepting the above stated equivalence, the value of g_{photo} for QWIP A have been calculated from noise measurements. Care has been taken in this case to ensure that the noise associated with the trapping and generation is measured, and not excess $1/f$ noise or another noise contribution.

In Fig. 33 we plot the noise gain for both QWIP A and an identical QWIP. For both devices the noise gain increases with increasing bias voltage.
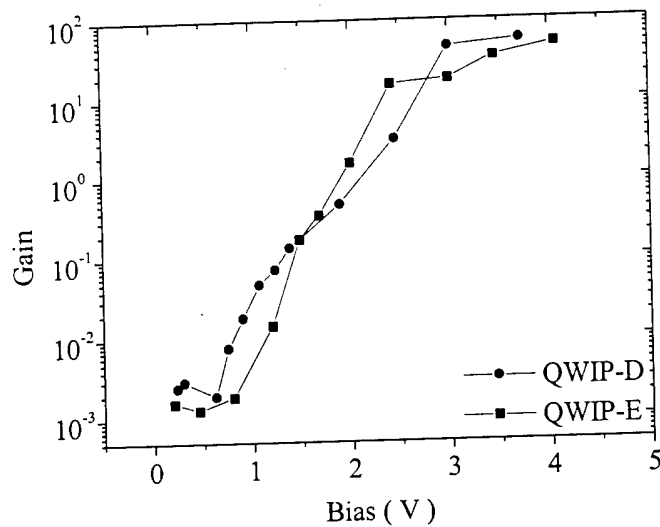
37

Fig. 33. Photoconductive gain as a function of bias for sample A and an identical sample at $T=77K$.

The electron trapping probability can be expressed in terms of the noise gain as[73]

$$p = \frac{1}{1+Ng} \tag{21}$$

where p is the electron trapping probability of a single well, N is the total number of wells of the device, and g is the gain. The trapping probability versus bias voltage is plotted in Fig. 34.
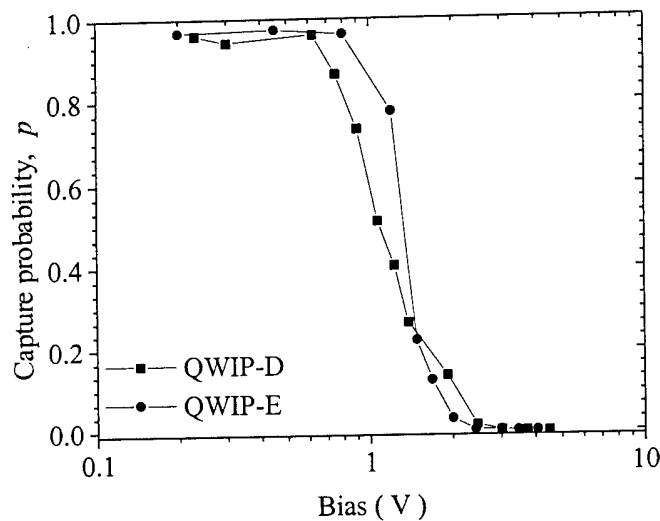
Fig. 34. Electron trapping probability versus applied bias voltage at $T=80K$.

Hence, the following pictures emerges. Electrons are thermally generated in the quantum wells, producing locally an excess electron density in the extended conduction states which subsequently spreads out into the MQW regions. The extended-state electron trajectory L_D, which might be affected by collision and/or tunneling (these noise measurements cannot discriminate between the two modes of transport), is terminated by trapping in a quantum well. At zero or low electric fields, this turns out (on average) to be same quantum-well that the

electrons originate from or the next-nearest neighboring well. At higher fields the electron trapping probability becomes smaller due to field-assisted lowering of the MQW barriers, thereby improving the coupling to the external circuit and increasing the gain and current noise level.

We define the electron lifetime in the conduction band to be τ_0, and in the ground state of the QW to be τ_w. We also define the total number of electrons in the conduction band to be P_o, and in the well is P_s. In equilibrium, the average number of electrons generated from the QW ground state should equal the average number of electrons recombining from the valence-band extended states. Thus:

$$G=R \text{ or } \frac{P_W}{\tau_W} = \frac{P_o}{\tau_o} \tag{22}$$

The particle number spectral density $\langle \Delta P \rangle^2 = S_P(f)\Delta f$ where $S_P(f)$ is according to van der Ziel:[74]

$$S_P(f) = 4G\frac{\tau^2}{1+\omega^2\tau^2} \tag{23}$$

where $\tau^{-1} \approx \tau_0 + \tau_W$, and G is the electron generation rate (s^{-1}) from the quantum well ground state to the conduction band extended state.

At low temperatures, the total number of holes in the conduction band is much smaller than the number of electrons in the QW ground state because the barriers are undoped. Therefore $\tau_0 \ll \tau_W$, resulting in $\tau \approx \tau_0$. This implies that the particle number spectral density at low frequencies is:

$$S_P(0) = 4G\tau_o^2 \tag{24}$$

In these n-type QWIPs with undoped barriers, the number of mobile electrons in the conduction band is equal to the number of electrons excited from the quantum well ground state (assuming there are no trap states emitting carriers). Therefore, dark current is defined as:

$$I_d = Aenv = ev\frac{P_o}{L} \tag{25}$$

Here v is the average electron velocity, n is the carrier concentration in the conduction band, L is the total device length.

Using the photoconductive gain , defined as $g=v\tau_o/L$, the dark current can also be written as:

$$I_d = ev\frac{P_o}{L} = eg\frac{P_o}{\tau_o} = egG \tag{26}$$

39

Current fluctuations are related to number fluctuations by Eq. 25, i.e. $\Delta I = \left(\dfrac{ev}{L}\right)\Delta P_o$. Thus the current noise spectral density S_i is defined as:

$$S_i = \langle \Delta i \rangle^2 = \left(\frac{ev}{L}\right)^2 \cdot S_P.$$

(27)

In the absences of an applied electric field, the diffusion length L_D is the distance a carrier diffuses before recombining into quantum well ground states. Therefore the current noise in the diffusion dominant regime can be expressed as:

$$S_i = 4e^2 G \left(\frac{\tau_o v}{L}\right)^2 = 4e^2 G \left(\frac{L_D}{L}\right)^2$$

(28)

When a sufficient bias is applied, transport is drift dominated and Eq. 28 no longer applies. By combining Eqs. 23, 26, and 27, the current noise spectral density can be expressed as:

$$S_i = 4\left(\frac{ev}{L}\right)^2 \frac{P_o^2}{G} = \frac{4I_d^2}{G}$$

(29)

As a result, the current noise in the drift dominant regime is proportional to the dark current squared. By substituting Eq. 26 into Eq. 29, it is obvious that the current noise power spectral density is proportional to the electron generation rate G:

$$S_i = 4g^2 e^2 G$$

(30)

Thus the noise current spectral density, i_n, defined by $\langle i_n \rangle^2 = S_i(f)\Delta f$, is given by:

$$i_n \big/ \sqrt{\Delta f} = 2ge\sqrt{G}$$

(31)

Detectivity $D^* = \dfrac{R_i \cdot \sqrt{area}}{i_n \big/ \sqrt{\Delta f}}$, was defined earlier. Substituting for R_i (Eq. 3) and i_n (Eq. 31) gives:

$$D^* = \frac{\eta \cdot \lambda \cdot \sqrt{area}}{2\sqrt{G}}$$

(32)

Thus a smaller generation rate is directly linked to a higher detector detectivity.

40

It is possible to model the generation rate if we assume the generation rate of electrons from the ground state of the quantum well is the same as the emission of electrons from a trap state to the conduction band,[75] so that:

$$1/\tau_{escape} = \nu_{th}\sigma_e N_c \exp(-\Delta E/kT) \tag{33}$$

where ν_{th} is the thermal velocity of the electron, ΔE is the energy from the QW ground state to the barrier conduction band, σ_e is the capture cross section of the trap, and N_c is the effective density of states in the conduction band. The generation rate density for the whole quantum well is defined as:

$$g = \frac{N_D}{\tau} = N_D \nu_{th} \sigma_e N_c e^{[-(\Delta E/kT)]} \tag{34}$$

The generation rate density can thus be written $g=C\exp(-\Delta E/kT)$, where C is an electron generation rate constant (in $cm^{-3} s^{-1}$). The total electron generation rate is:

$$G = NAL_w g, \tag{35}$$

where N is the number of periods of quantum wells, A is the area, and L_w is the quantum well width.

Furthermore, it is possible to model the expected capture cross-section by assuming a model of carrier recombination due to coulombic attraction to donor atoms. Thermally generated electrons move via drift or diffusion in the barrier region to a neighboring quantum well. These wells are doped with silicon donors to a concentration of $\sim 1\times10^{18} cm^{-3}$, which results in an inter-donor spacing of about 50 Å. Since the well width is only 50 Å, these donors basically form a monolayer thin plane of charge centers. The electrons approaching this monolayer with a thermal velocity determined by barrier parameters will interact with these silicon centers triggering a recombination process which results in the electrons reaching the E_1 bound state. Assuming ineffective screening of the silicon nuclei due to the two-dimensionality of the surrounding electron gas, we approximate the silicon pertubation potential[75] by $Zq/4\pi\varepsilon_0\varepsilon_r r$ where Z is the atomic number of silicon, equal to 14. The holes impinging on the silicon centers gain kinetic energy by crossing the well/barrier interface. Hence to determine the effective scattering cross section σ_e of the silicon centers embedded in the quantum wells, we can equate

$$\frac{Ze^2}{4\pi\varepsilon_o\varepsilon_r r} = \Delta E \tag{36}$$

The scattering cross section $\sigma_e=\pi r^2$ can then be calculated. This equation implies that electrons with energy higher than the right-hand side of Eq. 36 do not sense the pertubation potential and are not scattered. For a temperature of $T=77K$, and using $\varepsilon_r=13.7$ and $\Delta E = 138$ meV (see Fig. 31) for $In_{0.53}Ga_{0.47}As$, this model predicts a scattering cross section of $\sigma_e=3.6\times10^{-12} cm^2$.

The noise current spectral density versus dark current is plotted in Fig. 35 for QWIP-A.
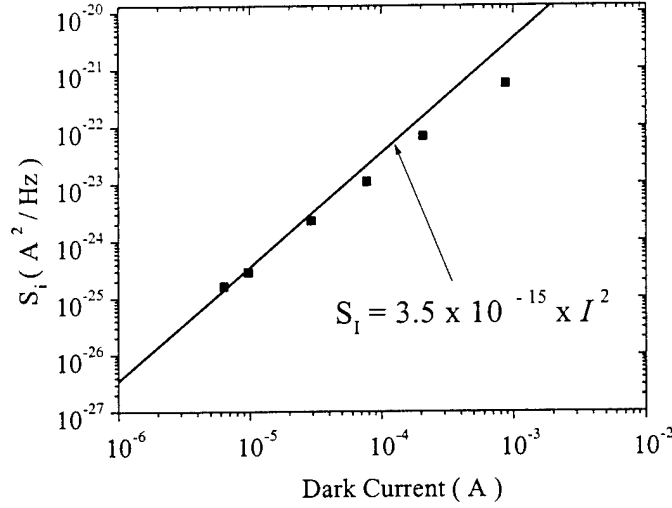
Fig. 35. Current noise spectral density versus dark current at T=80K for sample E.

The solid line illustrates the I^2 dependency predicted by Eq. 29. For high dark currents, the slight deviation of the measured curve from the I^2 dependence is attributed to an increase in the thermal generation rate. This effect is highlighted in Fig. 36 where the natural logarithm of the thermal generation rate G, calculated from Eq. 29, is plotted versus applied bias voltage. The calculated generation rate is 4×10^{22} cm^{-3} s^{-1}. The solid line is the best linear fit to ln(G) versus. bias and has a slope of 0.47 V^{-1}.
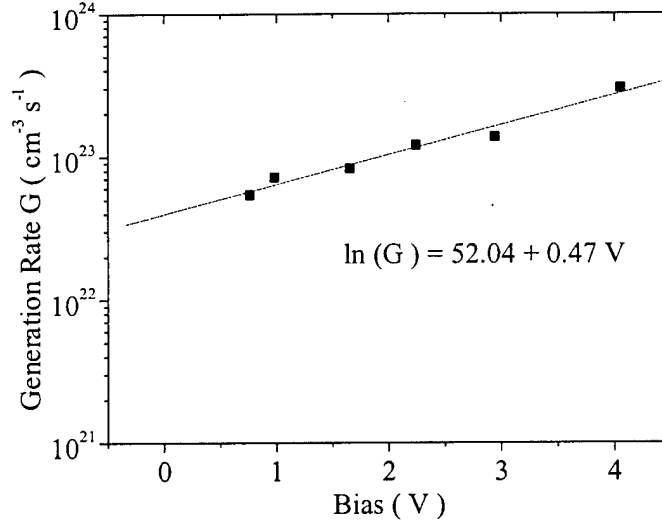

Fig. 36. Calculated thermal generation rate versus applied bias at T=77K for sample E.

From a simple charge balance model for heavily doped quantum wells it follows that:

$$G = e_n n_w = c_n n_w N_c \exp(-E_A/kT) = c_n n_d N_c \exp(-E_A/kT) \tag{37}$$

where e_n is the bound electron emission coefficient, c_n is the electron capture coefficient, n_w is the electron density in the quantum well ground state, N_c is the effective density of states of the continuum above the well, and E_{act} is the bound electron activation energy, equal to 138 meV for

42

these samples in equilibrium (Fig. 31). Upon applying bias, band bending will occur, leading to a lower activation energy because electrons can escape via the lowered side (in energy) of the quantum well. With a voltage drop V_W across a quantum well, a first order for an upper estimate of the effect is:

$$E_A = E_A^0 - eV_W, \tag{38}$$

where E_A^0 is the zero bias activation energy. Assuming a constant electric field throughout the device, including the quantum well regions,

$$V_W = V_W(L_p N), \tag{39}$$

where V is the applied bias voltage, and L_p is the length of a period. Solving Eqs. 38-41 results in:

$$\ln(G) = \ln(c_n n_d N_c) - E_A^0/kT + ewV/(kTL_p N) \tag{40}$$

predicting a linear dependence of $\ln(G)$ with V with a slope of 0.73, which is slightly larger than the measured value. This discrepancy may be due to the spatial dependence of bound electron generation. Theoretically, the highest electron concentration and thus generation rate is expected at or near the center of the quantum well where electrons will only experience a fraction of the band lowering. In addition, the electric field in the quantum well region may be lower than in the barrier. This will also lead to a smaller slope of $\ln(G)$ vs. V.

The generation rate constant C for sample E was found by fitting Eqs. 30 and 36 to the noise power spectral density shown in Fig. 35. The best is for $C=2.5\times10^{31}$ cm^{-3} s^{-1}. Fig. 37 shows the measured noise values (squares) versus applied bias voltage as well as the fit made using Eqs. 30 and 29. Note that Eq. 29 explains the magnitude for the noise very well for the drift dominated regime. The same value of C was used with Eq. 28 to fit the noise date is the diffusion dominant regime. The diffusion length L_D which gave the best fit for this value of C was $L_D=500$ Å, which is very similar to the diffusion length of 400 Å determined using Eq. 19.
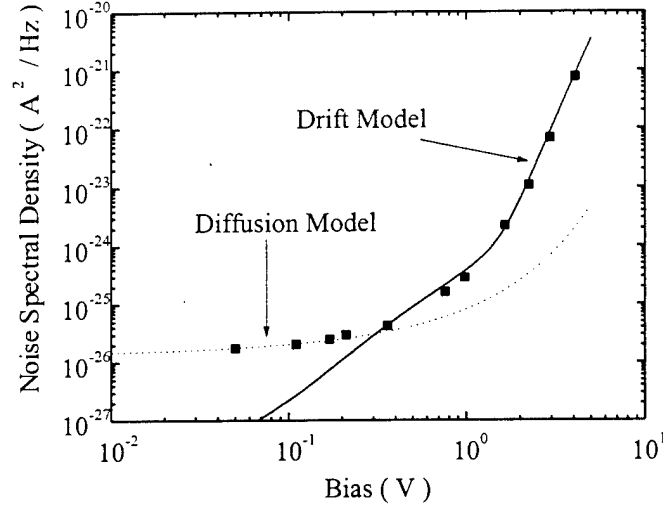
Fig. 37. Experimental and theoretical current noise spectral density versus bias voltage at T=77K for sample E.

A value of σ_ε=9.4×10^{-12} cm^2 is calculated for the capture cross section using Eq. 34 and C=2.5×10^{31} cm^{-3} s^{-1}. This calculation used N$_D$=8×10^{17} cm^{-3} and bulk values of N$_c$ and v_{th} for In$_{0.53}$Ga$_{0.47}$As. This agrees well (2.5× higher) with the values of 3.6×10^{-12} cm^2 obtained from the simple model of Eq. 36. The slightly higher measured scattering cross section may indicate the presence of some interface roughness-related or alloy scattering.

It is interesting to compare the thermal generation rate, gain, and capture probability measured for these samples with values previously published for AlGaAs/GaAs samples. For detectors with a similar peak absorption wavelength near 8 μm, Bosman et al.[72,73] have measured a generation/recombination rate of 1.5 x 10^{23} cm^{-3} s^{-1} in GaAs/ AlGaAs samples. Using Eq. 32, the 4× lower recombination rate for these InGaAs/InP samples should result in a 2× higher peak detectivity for detectors with similar areas at the same wavelength. This agrees fairly well with the published maximum peak detectivities for GaAs/AlGaAs detectors by Levine et al.[7] (1×10^{10}) and Claiborne et al.[76] (3×10^{10}) as compared to the peak detectivities for InGaAs/InP detectors in this work (6×10^{10}) and Gunapala et al.[77] (9×10^{10}). It is hypothesized here that the recombination rates are larger in GaAs/AlGaAs heterostructures due to larger scattering cross sections from larger interface roughness in a ternary material or the presence of aluminum related DX-center traps.

A comparison of the photoconductive gain measured for different QWIP materials is shown in Fig. 38. As discussed above, the higher gain in InP-barrier QWIPs is probably due to the longer carrier lifetime (because of a lower recombination rate) and higher drift velocity in the InP barriers, and perhaps a decrease in the number of scattering centers due to the high quality of the binary barrier material.
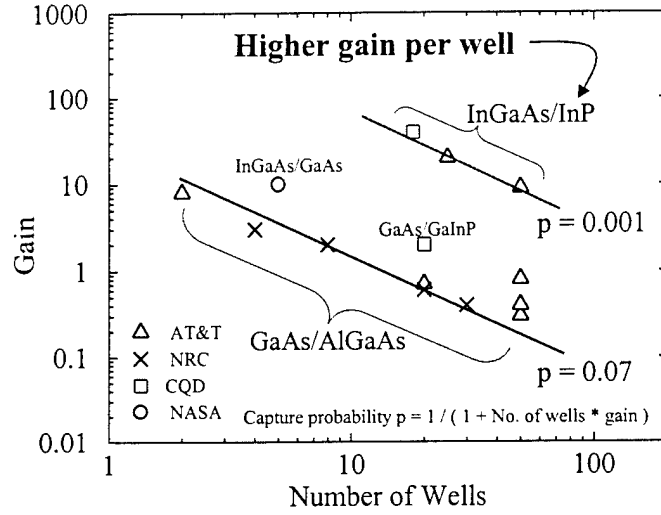
Fig. 38. Photoconductive gain versus number of quantum wells for various QWIP systems.

The increased gain results in a higher detector responsivity. The responsivity for sample A is larger compared with GaAs/AlGaAs devices by Gunapala et al.[78] This is shown in Fig. 39.
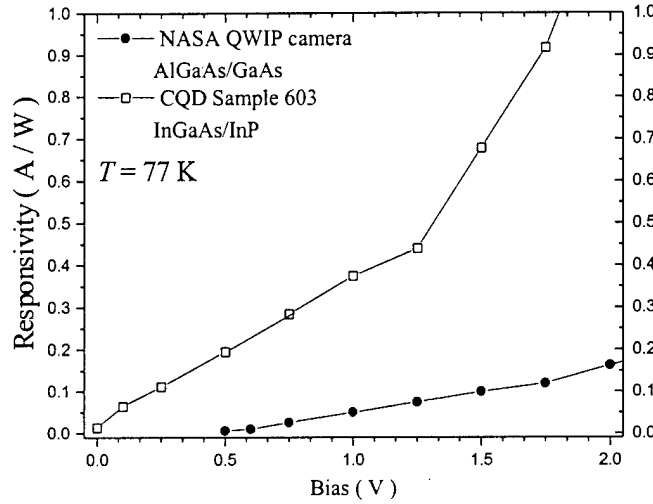
Fig. 39. InGaAs/InP QWIP (sample E) responsivity compared to GaAs/AlGaAs QWIP of Ref. [78].

3.4. GaInAsP/InP QWIPs (λ = 8–20 μm)

In this section, we report the first detailed measurements performed on QWIPs fabricated from n-type GaInAsP quantum wells and InP barriers grown by metalorganic chemical vapor deposition (MOCVD).

Three QWIP devices were studied and the device parameters are listed in Table 9, where L_B represents the barrier width, L_W is the well width, and N_D denotes the donor doping concentration of the quantum wells.

45

Table 9. Device parameters for the measured QWIPs.

QWIP	A	B	C
Barrier material	InP	InP	InP
L_B	500 Å	500 Å	500 Å
Well material	$In_{0.625}Ga_{0.375}As_{0.8}P_{0.2}$	$In_{0.73}Ga_{0.27}As_{0.575}P_{0.425}$	$In_{0.53}Ga_{0.47}As$
Well bandgap	1.3 μm	1.55 μm	1.65 μm
L_W	65	65	60
N_D (n_s)	1.7×10^{17} cm^{-3} (1.1×10^{11} cm^{-2})	1.7×10^{17} cm^{-3} (1.1×10^{11} cm^{-2})	1.7×10^{17} cm^{-3} (1.0×10^{11} cm^{-2})
Periods	20	20	20

The MQW structures were grown in a MOCVD system. The growth chamber was fitted with a Alcatel 2063CP+ pump to handle the gas load. The group V source materials were 100% AsH_3 and PH_3, and the group III source materials were trimethylindium and triethylgallium. All metalorganic were introduced into the growth chamber using a hydrogen carrier gas. Flow rates were regulated by mass flow controllers. The substrates were inductively heated using an RF coil and a graphite susceptor. As a result the sample's temperature was regulated to within ± 1.5 °C, with excellent reproducibility from run to run.

All samples were grown at a substrate temperature of 480°C on semi-insulating (100) InP wafers. The growth rates of InP, GaInAs, GaInAsP (1.3 μm) and GaInAsP (1.5 μm) were 150, 300, 230, and 260 Å/min respectively. The wells of the MQW structure were silicon doped using silane to a level of 1.7×10^{17} cm^{-3}. Top and bottom contact layers of 0.5 μm-thick $In_{0.53}Ga_{0.47}As$ doped $n = 1 \times 10^{18}$ cm^{-3} were grown for ohmic contacts.

Arrays of 400 × 400 μm^2 mesas were etched through the photosensitive MQW region using a Plasma-Therm 770 ECR/RIE etch system. A mix of $H_2/Ar/Cl_2$ gases was used. Finally, Ti/Pt/Au ohmic contacts were evaporated onto the top and bottom contact layers. The dark current versus bias voltage characteristic at $T = 80$ K of typical detectors for each of the three samples is shown in Fig. 40.
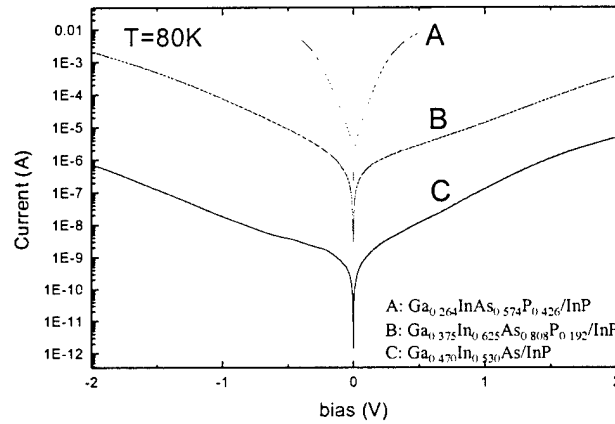

Fig. 40. The dark current curves of samples A, B, and C measured at 80 K.

The relative responsivity spectra for these three samples were collected using a Mattson Galaxy 3000 FTIR. The responsivity spectrum of the three samples is shown in Fig. 41. For a bias of −1 V (mesa top negative), the 50% cutoff wavelengths for the three samples A-C were 9.3, 10.7, and 14.2 μm respectively. The peak and cutoff wavelengths and linewidth $\Delta\lambda/\lambda$ for the three samples are given in Table 10. The switch from a bound-to-bound to a bound-to-continuum transition between samples B and A is evident.
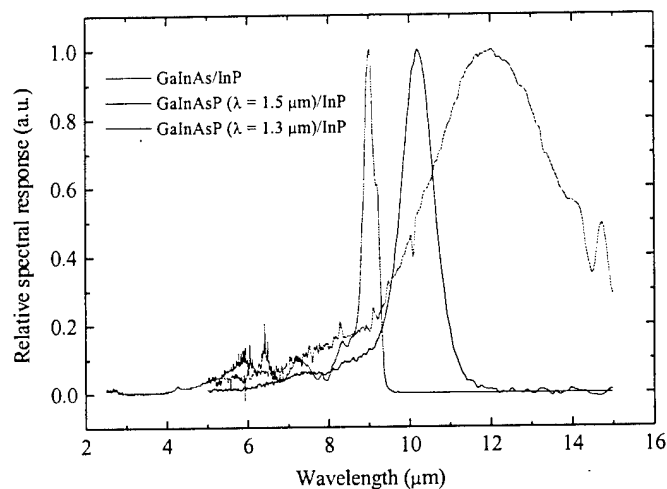
Fig. 41. The relative spectral responses for samples A, B, and C.

Table 10. Spectral response parameters for the three samples studied.

Sample	Peak wavelength (μm)	Cutoff wavelength (μm)	FWHM (Δλ/λ)
A	12.03	14.24	36%
B	10.2	10.7	10%
C	9	9.25	5.5%

The absolute responsivities were measured by using a calibrated blackbody source. The detectors were back illuminated through a 45° polished facet. The bias dependence of the responsivity was measured for all three samples. The two samples B and C were measured at T = 80 K. Unfortunately, the responsivity of sample A was too low to be measured at T = 80 K; instead, the responsivity of this sample was measured at T = 30K. The peak responsivity for all three samples is shown in Fig. 42.

Fig. 42. The peak responsivity measured as a function of bias for samples A, B, and C.

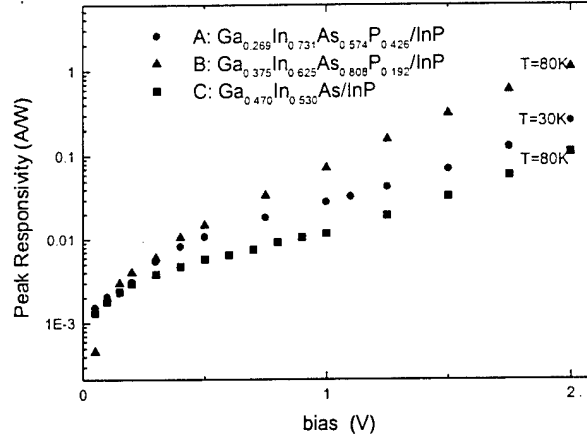The peak responsivity at −1 V of the three samples A–C were 28.1, 71.8, and 11.8 mA/W, respectively. The noise current i_n, of samples B and C were measured at $T = 80$ K and sample A was measured at $T = 30$ K. The noise was measured using a spectrum analyzer and found to be $i_n = 10$ pA, 4.4 pA, and 62 fA, respectively for samples A–C. The peak detectivities, $D*_\lambda$ can now be calculated from $D_\lambda^* = R\sqrt{A\Delta f} / i_n$ where $A = 1.6 \times 10^{-3}$ cm^2 is the device area and $\Delta f = 1$ Hz is the bandwidth.

At an operating bias of $V_B = -1$ V and $T = 80$ K the detectivity for samples B and C are $D* = 2 \times 10^8$ and 8×10^9 cm $\sqrt{Hz}$ W^{-1}, respectively. The detectivity of the sample A at $T = 30$ K is $D* = 1.1 \times 10^8$ cm $\sqrt{Hz}$ W^{-1}. The detectivity of all three samples as a function of bias is shown in Fig. 43.
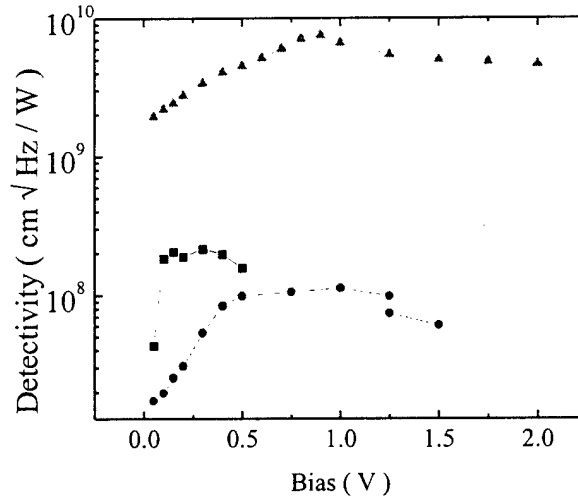
Fig. 43. Specific detectivity as a function of bias for samples A (circles) , B (squares), and C (triangles).

Using the spectral response data obtained for these samples, it is possible to estimate the conduction band offset for the $Ga_xIn_{1-x}As_yP_{1-y}$/InP heterojunction. The cutoff wavelength for samples A, B, and C correspond approximately to the energy separation $\Delta E = E_2 - E_1$ for the three quaternary compositions: sample A $(x, y) = (0.27, 0.575)$, sample B $(x, y) = (0.375, 0.80)$, and sample C $(x, y) = (0.47, 0)$. The energies of the first and second allowed states for these

GaInAsP/InP samples can be calculated for several possible conduction band offsets using the well widths given in Table 9. In Table 11, the conduction band offset that best fits the cutoff wavelength observed in Fig. 41 is listed. As is seen from Table 11, the conduction band offset to bandgap ratio ($\Delta E_c/\Delta E_G$) is nearly constant for all three samples, with an average value of ~ 0.32. This value for the GaInAsP/InP conduction band offset is smaller than the previously reported value of 0.40.[79,80]

Table 11. The conduction band offset for the three samples studied.

Sample	Cutoff wavelength (μm)	Conduction band offset (%)
A	14.24	32
B	10.7	30
C	9.25	33

3.5. Multispectral QWIPs

As we have shown earlier in this section, QWIPs lattice-matched to InP substrate can be used for detection in the MWIR, LWIR, and VLWIR infrared spectral regions. Fig. 44 shows the combined relative spectral responses for samples A, B, C, and D as a function of wavelength. The MWIR and LWIR regions of high atmospheric transmission are indicated by arrows. Multispectral detectors lattice-matched to GaAs substrate, using the GaAs/AlGaAs and InGaAs/AlGaAs systems have been previously reported. In this section, we report the first multispectral detectors on InP substrate.
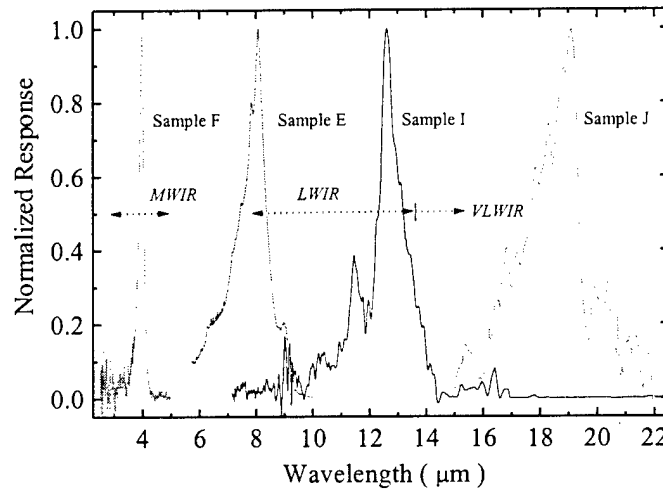
Fig. 44. QWIP detectors lattice matched to InP can cover the entire range from 3-20 μm, as shown in this figure using the spectral response for samples A, B, C, and D.

A sample (wafer K) was grown for multispectral absorption in both MWIR and LWIR regions by including multiple quantum wells of both InGaAs/InAlAs and InGaAs/InP. The QWIP structure was grown on (100) oriented semi-insulating (Fe-doped) InP substrates. The first layer is a 1 μm thick buffer layer of n+ InGaAs doped with silicon to $n=1\times10^{18}$ cm^{-3}. This served a bottom contact. Next grown was two series of MQWs. The first consisted of 21

barriers layers of InP (500 Å) confining 20 wells of $In_{0.53}Ga_{0.47}As$ (55 Å). The second consisted of 21 barrier layers of $In_{0.52}Al_{0.48}As$ (350 Å) confining 20 wells of $In_{0.53}Ga_{0.47}As$ (35 Å). Last grown was a 0.5 μm top contact layer of n+ $In_{0.53}Ga_{0.47}As$ (silicon doped to $n=1x10^{18}$ cm^{-3}). For this sample, the 2 Å nearest each barrier remained undoped. The remainder of the well was doped to a concentration $n=5x10^{17}$ cm^{-3}.

Detectors from wafers K were fabricated using the Plasma-Therm ECR/RIE dry etching system. Because the mask utilized in this work allows only one contact to be made to the mesa, the two MQW detectors are placed in series. At low biases, the electric field is applied mostly across the lower-resistance InGaAs/InP MQW. At higher biases, the electric field is applied across both MQWs, but the InGaAs/InP MQW is under such high field that no response is observed. This is because most carriers in the ground states of the InGaAs/InP quantum wells tunnel out before absorption occurs. A schematic of the processed device is shown in Fig. 45.
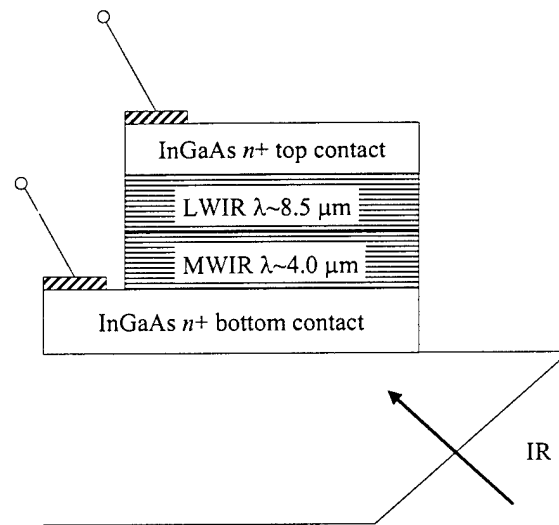

Fig. 45. Multispectral QWIP design used for measuring sample K.

The spectral response of detectors from wafer K are shown in Fig. 46 for several biases. For biases less than 10 V, the photoresponse in the 3-5 μm region is too noisy to resolve. For biases greater than ~ 7 V, the photoresponse in the 8-9 μm region is no longer observed.
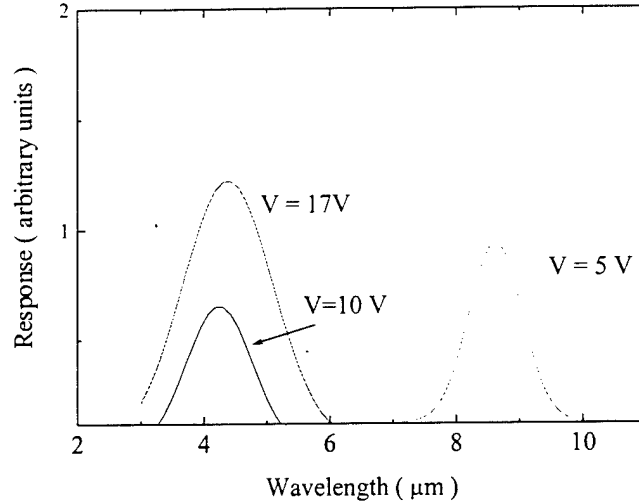
Fig. 46. Response for wafer K at T=77K for several biases. For V< 7 volts, only one peak at ~ 8.5 µm is observed. For higher biases, a peak at ~ 4 µm is measured.

Because only one mask set was available for this work, the multispectral QWIP presented in this section operates as a voltage tunable detector, rather than a true simultaneous multi-spectral detector. Nonetheless, the feasibility of integrating mid-wavelength, long-wavelength, and/or very long-wavelength QWIPs based on InP into a multispectral imaging array has been demonstrated. Much more work is necessary in order to determine the best QWIP design for a particular set of wavebands. Because of the preliminary nature of these results, it is not possible to compare two-color detectors based on InP and GaAs substrates. However, it is useful to note that $In_{0.3}Ga_{0.7}As/Al_{0.38}Ga_{0.62}As$ quantum wells are required for MWIR detectors based on GaAs substrate. These quantum wells are mismatched by ~ 1.43% to the GaAs substrate. Therefore, for multispectral absorption where both wavebands ∆λ lie in the 3-5 µm infrared region, $In_{0.53}Ga_{0.47}As/In_{0.52}Al_{0.48}As$ QWIPs should offer improved performance due to their lattice-matched nature with the InP substrate.

4. Conclusions

We have characterized and optimized the performance of QWIPs fabricated from quantum wells or barriers of $Ga_xIn_{1-x}Al_{1-x-y}As$ or $Ga_xIn_{1-x}As_yP_{1-y}$ material and made comparisons with that achieved with the more mature $GaAs/Al_xGa_{1-x}As$ device design. In order to demonstrate new functionality, such as the possibility of multispectral detection, we have investigated several different designs based on heterostructures of GaAs/GaInP, InGaAs/InP, InGaAs/InAlAs, and AlGaInAs/InP.

We are able to deduce from the QWIP devices fabricated from GaAs/GaInP several important parameters describing this heterostructure system. A precise value of for the conduction band discontinuity of 122 meV ± 2 meV was calculated. A drift mobility of 1000 cm^2 V^{-1} s^{-1}, saturation velocity of 1.5 x 10^5 cm^{-1}, and carrier lifetime of ~ 5 ps have also been extracted from the current-voltage curves. Using GaAs/GaInP QWIP wafers grown as part of this work, we obtained the first infrared images from a QWIP array made from a material other that GaAs/AlGaAs. Although it is clear that the conduction band offset in this system is too small for 8-12 µm devices, excellent very-long-wavelength infrared (VLWIR) detectors were produced with performance equivalent to GaAs/AlGaAs detectors at the same wavelength.

Three identical GaInAs/InP QWIP series ($\lambda = 9$ μm) were grown by LP-MOCVD with three different quantum well doping densities. The optimal detectivity came from the series with $N_D = 5.0 \times 10^{17}$ cm^{-3}. This series had a responsivity of 33.2 AW^{-1} and operated with a detectivity of 3.5×10^{10} cmHz$^{1/2}$W^{-1} at a bias of 0.75 V. This responsivity is to our knowledge the higest value reported for any QWIP in the $\lambda = 8$–9 μm range.

We also have conducted the first complete measurements of the noise performance of InGaAs/InP QWIPs. These noise spectroscopy techniques provide information on the photoconductive gain and quantum well capture probability in this heterostructure. The average electron diffusion length and thermal generation rate have also been calculated. InGaAs/InP devices grown by gas-source MBE demonstrated improved detectivity and responsivity in comparison to equivalent GaAs/AlGaAs detectors. The noise measurements quantitatively captures these improvements by demonstrating the larger photoconductive gain, and thus larger responsivity, than is obtained using InP barriers instead of AlGaAs.

We presented optimization of the device design for InGaAs/InAlAs QWIPs for mid-wavelength infrared detection. These MWIR detectors demonstrate high detectivity, and have a constant responsivity up to T=200 K. The fact that they are lattice-matched to InP has allowed us to demonstrate the first InP-based multispectral detector for 3-5 and 8-9 μm detection. We additionally presented QWIPs fabricated from the AlGaInAs/InP material system that is sensitive to the spectral region between $\lambda = 8$–20 μm when the Al mole fraction is varied from 0–15 %.

Lastly, we have demonstrated the first preliminary QWIP detectors using the quaternary InGaAsP/InP materials system growth by MOCVD. By increasing the bandgap from ternary InGaAs to quaternary InGaAsP we have shifted the responsivity out to longer wavelengths resulting in cutoff wavelengths of 10.7 and 14.2 μm for As mole fractions of 0.80 and 0.57, respectively. For the device with a 10.7 μm cutoff wavelength, we have observed responsivity as large as 1.09 A/W at a bias of 2 V. The conduction band offset for these samples is ~ 0.32, smaller than the typically reported value of 0.40.

5. Future Work

Nearly all QWIPs produced are fabricated on GaAs or InP substrates, which are the obvious choices for III-V–based QWIPs. However, the readout and integration circuitry for FPAs—QWIP and otherwise—is Si-based. A technique like flip-chip bonding is thus necessary to mate the III-V optical device and the Si circuitry.[81] Many advantages exist if the QWIP could be directly grown on Si substrate, such as higher thermal conductivity and mechanical strength, the availability of large-area substrates, and more straightforward integration and cheaper FPAs.[82] The major obstacle to overcome for this to occur is the large mismatch between Si and the III-V materials.

There have been demonstrations of QWIPs made from GaAs/AlGaAs grown directly on Si,[83,84] but as of yet no InP-based QWIPs on Si have been produced. Devices based on InP are expected to be more difficult to produce because the lattice mismatch between it and Si is larger than the mismatch between GaAs and Si. Nevertheless, based on the superior responsivity of GaInAs/InP QWIPs and the usefulness of the monolithic integration of QWIPs with Si-based readout circuitry, our goal is to produce GaInAs/InP QWIPs directly on Si substrate.

5.1. Growth of lattice mismatched epilayers

When a mismatched epilayer is deposited on top of a substrate, it initially matches the lattice constant of the substrate through compression or tension of the crystal. Thus the epilayer lattice squeezes or stretches to fit the substrate lattice, which creates strain forces inside the epilayer crystal. This is valid up until the epilayer crystal is thick enough that it cannot sustain any more additional strain, and thus it finds another mechanism to relax the strain: the creation of misfit dislocations. The threshold thickness where this occurs is called the critical thickness, and represents the point where the epilayer crystal relaxes back to its free-standing lattice constant and all strain forces are absolved with the formation of these misfit dislocations.[85,86]

From the standpoint of device fabrication, the existence of misfit dislocations are unwanted because they seriously degrade performance.[87] The dislocations act as capacitors and attract charge carriers from the surrounding area, which interrupt the normal carrier distribution in a device and hence hampers its operation. For this reason it is desirable to prevent dislocation formation by keeping all epilayers below their respective critical thicknesses.

On planar substrates with no means for reducing strain on deposited layers, the critical thickness can be expressed by at least two formulas, the Matthews–Blakeslee formula,[85]

$$d_c = \frac{b}{8\pi(1+v)f}\ln\left(\frac{d_c}{b}+1\right) \tag{41}$$

where d_c is the critical thickness, b is the Burgers vector length, v is Poisson's ratio, and f is the lattice mismatch, and the People-Bean formula,[86]

$$d_c = \frac{(1-v)b^2}{8\pi(1+v)wf^2}\ln\left(\frac{d_c}{b}\right) \tag{42}$$

where w is the dislocation separation. The former is based on the assumption that dislocations form immediately when the hypothetical critical thickness is reached and are evenly spaced apart, while the latter is based on the assumption that dislocations form individually and are isolated from each other. Usually the critical thicknesses calculated with the People–Bean model are significantly greater than those calculated with the Matthews–Blakeslee model.

In the case of depositing III-V alloys directly on Si, the critical thickness is minute. The lattice mismatch between GaAs and Si is 4.1%, while the mismatch between InP and Si is 8.1%. In both cases the critical thickness is less than one monolayer, so the onset of misfit dislocations happens almost as soon as the layer is deposited.

During two-dimensional Frank–van der Merwe growth, misfit dislocations usually originate from threading dislocation segments that propagate to the epilayer surface up from the epilayer-substrate interface.[88] The threading dislocations can either be intrinsic (formed from impinging dislocations that favorably interact and do not annihilate each other) or extrinsic (already existing in the substrate and transferred to the epilayer.) The density of misfit dislocations can be reduced by either decreasing the number of dislocations at the surface or bending away the dislocations as they travel upward.

One technique used to reduce the dislocation density in a mismatched epilayer is to ease the strain with a series of composition-graded layers, as shown in Fig. 47(a). Instead of having one large mismatch between substrate and epilayer, there is a smaller mismatch between adjacent

epilayers. This produces a smaller number of dislocations at each interface, plus gives the possibility of the misfit dislocations gliding along the lower interfaces, away from the surface. Another technique is the implementation of strained-layer superlattices, pictured in Fig. 47(b). The large number of interfaces act as a barrier to the upward propagation of dislocations and force them to bend and travel parallel to the interface, where the dislocations can terminate at the edge of the structure instead of its surface. For this reason strained-layer superlattices are known as dislocation filters.
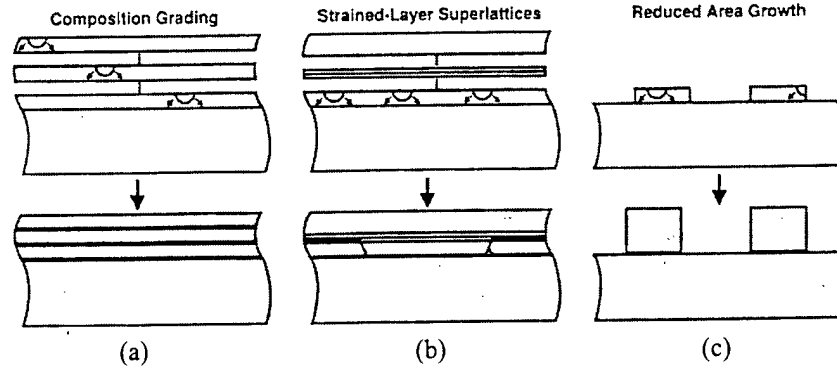

Fig. 47. Three techniques used to reduce the dislocation density in mismatched epilayers: (a) composition gradings, (b) strained-layer superlattices, and (c) reduced area growth.

The third technique is reduced area growth,[89] shown in Fig. 47(c). Instead of growing on a large substrate, the substrate can be patterned with mesas or ridges, performed by wet- or dry-chemical etching, thereby reducing the effective area on which epitaxy takes place. An advantage of this technique is that a dislocation is much more likely to reach the edge because of the shorter path it must travel. Another advantage of growing in a reduced area is that mechanisms that depend on area, such as dislocation multiplication, are sharply curtailed.[90]

This is shown mathematically[91] by first expressing the linear density of dislocations n as

$$n = \frac{\delta}{b_{eff}} \tag{43}$$

where b_{eff} is the Burgers vector length along the dislocation direction and δ is the plastic deformation given by

$$\delta = \rho_{ext} b_{eff} l_{mean} \eta \tag{44}$$

where ρ_{ext} is the area density of extrinsic dislocation sources, l_{mean} is the mean length of the dislocations, and η is the fraction of the extrinsic sources actually producing a dislocation. For a square mesa of side L, $l_{mean} \approx L/2$, and combining this with Eqs. 43 and 44 yield

$$n \approx \frac{\rho_{ext} \eta L}{2} \tag{45}$$

This equation shows that the density of misfit dislocations is linearly dependent on the mesa size: the smaller the mesa, the lower the dislocation density. This translates into larger critical thicknesses for growth on patterned substrates.

A disadvantage of this technique is the alteration of growth rate[92] and composition[93] close to the mesa edge. Because an adatom does not immediately incorporate into the lattice, it has the opportunity to laterally diffuse on top the surface before incorporation. When this occurs on a mesa, off-plane facets form at the edges where an adatom prefers to incorporate. Hence at the mesa edges, the growth rate is enhanced. Adatoms can also laterally diffuse from the dielectric to the semiconductor if the mesa is formed by openings in a dielectric mask instead of etching. Compositional changes occur near the mask edge in alloys containing two or more group III species, e.g. GaInAs, because the lateral diffusion rates of Ga and In are different, and so the composition of the ternary throughout the whole mesa will not be uniform. These factors must be taken into account when performing localized epitaxy.

5.2. Growth of GaInAs/InP QWIP structures on Si

The crucial part of a QWIP is its absorption region, which is a SL quantum well region. The interfaces between the well and barrier in this region must be abrupt for absorption to occur. If not, carriers could more easily spill out of the well, which would contribute to the dark current, or they could more easily fall back into the well, which would lower the photocurrent.

Another consideration for mismatched structures is that the dislocation density must be kept to a minimum. As mentioned above, these threading dislocations act as conduction pathways, and if their density is high enough, the series resistance of the detector could dramatically drop. Since a small resistance leads to a large dark current, it is imperative that the resistance be kept large.

Although growing on a planar substrate is simpler and more straightforward, the best way to reduce threading dislocations is with the use of localized epitaxy. By creating a patterned substrate prior to epitaxy, not only will the growth area be confined, but each individual device will already be defined by the pattern, eliminating the need for etching afterwards. The proper growth conditions for epitaxy must be found to yield epilayers with uniform thicknesses and abrupt interfaces. This becomes especially important as the fabrication is advanced from single detectors to focal plane arrays, where the array performance is critically dependent on the detector uniformity.

6. CQD QWIP publications

1. J. Hoff, C. Jelen, S. Slivken, E. Michel, O. Duchemin, E. Bigan, M. Razeghi, G. Brown and S.M. Hegde, "Intersubband hole absorption in GaAs-GaInP Quantum Wells grown by Gas Source Molecular Beam Epitaxy, " *Appl. Phys. Lett.* **65**, 1130 (1994).

2. J. Hoff, S. Kim, M. Erdtmann, R. Williams, J. Piotrowski, E. Bigan, M. Razeghi and G. Brown, "Background Limited Performance in p-doped $GaAs/Ga_{0.71}In_{0.29}As_{0.39}P_{0.61}$ Quantum Well Infrared Photodetectors," *Appl. Phys. Lett.* **67**, 22 (1995).

3. J. Hoff, E. Bigan, G. J. Brown, and M. Razeghi, "Aluminum-free Quantum Well Intersubband Photodetectors with p-type GaAs Wells and lattice-matched ternary and quaternary barriers", *Proc. SPIE* **2397**, 445 (1995).

4. J. Hoff, X. He, M. Erdtmann, E. Bigan, M. Razeghi, and G.J. Brown, "p-dopedGaAs/$Ga_{0.51}In_{0.49}P$ quantum well intersub-band photodetectors," *J. Appl. Phys.* **78**, 2126 (1995).

5. J. Hoff, C. Jelen, S. Slivken, E. Bigan, M. Razeghi, and G.J. Brown, "Analysis of Spectral Response in p-type GaAs/GaInP QWIPs," *Superlattices and Microstructures* **8**, 249 (1995).

6. "Growth and Characterization of GaInP/GaAs System for Quantum Well Infrared Photodetector Applications," Chapter 2 in *Long Wavelength Infrared Detectors*, M. Razeghi, Editor, Gordon and Breach Publishers, Inc., published 1996.

7. J. Hoff, J. Piotrowski, E. Bigan, M. Razeghi, and G.J. Brown, "Background limitedperformance in p-doped quantum well intersubband photodetectors," International Symposiumon Compound Semiconductors (ISCS-22), Cheju Island, Korea, Int. Phys. Conf. Ser. No. 145, J.C. Woo and Y.S. Park (eds.), pp. 1109-1114, IOP Publishing, 1996.

8. J. Hoff, C. Jelen, S. Slivken, G. J. Brown, and M. Razeghi, "Optical Absorption and Photoresponse in fully Quaternary p-type Quantum Well Detectors," *Proc. SPIE* **2685**, 62 (1996).

9. M. Razeghi, J. Hoff, M. Erdtmann, S. Kim, D. Wu, E. Kaas, C. Jelen, S. Slivken, I. Eliashevich, J. Diaz, E. Bigan, G.J. Brown, S. Javadpour, "MOCVD Growth of $Ga_{1-x}In_xAs_yP_{1-y}$-GaAs Quantum Structures," Heterostructure Epitaxy and Devices, Smolenice Castle, Slovakia, NATO 2nd International Workshop on Heterostructures Epitaxy and Devices (HEAD '95), J. Novakand A. Schlachetzki (eds.), p. 229-245, Kluwer Academic Publishers, 1996.

10. M. Razeghi, C. Jelen, S. Slivken and J. Hoff, "III-V interband and intraband far-infrareddetectors," 23rd International Symposium on Compound Semiconductors, St. Petersburg, Russia, Proceedings: Vol. 155, pp. 405-410, 1996.

11. J. R. Hoff, M. Razeghi and G. Brown, "Effect of the spin split-off band on optical absorption InP-type $Ga_{1-x}In_xAs_yP_{1-y}$ quantum-well infrared detectors," *Phys. Rev. B* **54**, 10773 (1996).

12. C. Jelen, S. Slivken, G. J. Brown, and M. Razeghi, "GaAs/GaInP Quantum Well Intersubband Photodetectors for Focal Plane Array Infrared Imaging," Materials Research Society Symposium, Boston, MA, Proceedings: Infrared Applications of Semiconductors-Materials, Processing and Devices, Vol. 450, pp. 195-199, 1996.

13. M. Razeghi, J. D. Kim, C. Jelen, S. Slivken, E. Michel, H. Mohseni, J. J. Lee, J. Wojkowski, K. S. Kim, H. I. Jeon, and J. Xu, "Infrared Imaging Arrays Using Advanced

III-V Materials and Technology," Advanced Workshop on Frontiers in Electronics (WOFE), Tenerife, Spain, Proceedings, pp. 57-64, 1997.

14. C. Jelen, S. Slivken, J. Hoff, M. Razeghi, and G. Brown, "Aluminum free GaInP/GaAs Quantum Well Infrared Photodetectors for Long Wavelength Detection," *Appl. Phys. Lett.* **70**, 360 (1997).

15. C. Jelen, S. Slivken, G. J. Brown, and M. Razeghi, "Very Long Wavelength GaAs/GaInP Quantum Well Infrared Photodetectors," *Proc. SPIE* **2999**, 144 (1997).

16. C. Jelen and M. Razeghi, "InP-based Multi-Spectral Quantum Well Infrared Photodetectors," International Semiconductor Device Research Symposium (ISDRS '97), Charlottesville, VA, Proceedings, pp. 599-602, 1997.

17. C. Jelen, S. Slivken, T. David, G. Brown, and M. Razeghi, "Responsivity and Noise Performance of InGaAs/InP Quantum Well Infrared Photodetectors," *Proc. SPIE* **3287**, 96 (1998).

18. C. Jelen, S. Slivken, T. David, M. Razeghi and G. J. Brown, "Noise performance of InGaAs/InP quantum well infrared photodetectors," *IEEE J. Quant. Electron.* **34**, 1124 (1998).

19. C. Jelen, S. Slivken, V. Guzman, M. Razeghi, and G. Brown, "InGaAlAs/InP Quantum Well Infrared Photodetectors for 8-20 μm Wavelengths," *IEEE J. Quant. Electron.* **34**, 1873 (1998).

20. C. Jelen, S. Slivken, G.J. Brown, and M. Razeghi, "Multi-color 4-20 μm In-P-based QuantumWell Infrared Photodetectors," *Proc. SPIE* **3629**, 147 (1999).

21. C. Jelen and M. Razeghi, "AlGanInAs/InP-based Quantum Well Infrared Photodetectors," *Opto-Electronics Review* **7**, 1 (1999).

22. M. Erdtmann, A. Matlis, C. Jelen, M. Razeghi, and G. Brown, "High-responsivity GaInAs/InP quantum well infrared photodetectors grown by low-pressure metalorganic chemical vapor deposition", *Proc. SPIE* **3948**, 220 (2000).

23. M. Erdtmann, J. Jiang, A. Matlis, A. Tahraoui, C. Jelen, M. Razeghi, and G. J. Brown, "Growth and optimization of the GaInAsP/InP material system for quantum well infrared photodetector applications", *Proc. SPIE* **3948**, 227 (2000).

24. M. Erdtmann, J. Jiang, C. Jelen, M. Razeghi, G. J. Brown, and Y. S. Park, "High-responsivity GaInAs/InP quantum well infrared photodetectors ($\lambda = 9$ μm) grown by low-pressure metalorganic chemical vapor deposition", submitted to *Appl. Phys. Lett.*

25. M. Razeghi, M. Erdtmann, C. Jelen, J. Diaz and G.J. Brown, "Long-Wavelength Quantum Well Infrared Photodetectors," to appear in special issue of *Defence Science Journal* section on "Materials and Devices for Night Vision & IR."

26. M. Razeghi, M. Erdtmann, C. Jelen, J. Diaz, F. Guastavinos, G. J. Brown, and Y. S. Park, "Quantum well infrared photodetector ($\lambda = 3$–20 μm) focal plane arrays: monolithic integration with Si-based read-out integrated circuitry for low cost and high performance", to appear in *Proc. SPIE*.

7. References

1. L.West and S.Eglash, Appl.Phys.Lett.**46**, 1156 (1985).
2. W.A.Beck and T.S. Faska, SPIE **2744** 193 (1996)
3. C. Jelen, S. Slivken, V. Guzman, M. Razeghi, and G. J. Brown, *IEEE J. Quant. Electron.* **34**, 1873 (1998).
4. C. Jelen, S. Slivken, T. David, G. Brown, and M. Razeghi, *Proc. SPIE* **3287**, 96 (1998).
5. S. D. Gunapala, B. F. Levine, D. Ritter, R. Hamm, and M. B. Panish, *Appl. Phys. Lett.* **58**, 2024 (1991).
6. J. Y. Andersson, L. Lundqvist, Z. F. Paska, K. Streubel, and J. Wallin, *Proc. SPIE* **1762**, 216 (1992).
7. B. Levine, J. Appl. Phys. **74**, R1 (1994)
8. C.Chen, K.Choi, M.Tidrow, D. Tsui, Appl. Phys. Lett. **68** 1446 (1996).
9. G.Hasnain, B. Levine, D. Sivco, A. Cho, Appl. Phys. Lett. **56** 770 (1990).
10. L. Esaki and H. Sakaki, *IBM Tech. Disc. Bull.* **20**, 2456 (1977).
11. B. F. Levine, K. K. Choi, C. G. Bethea, J. Walker, and R. J. Malik, *Appl. Phys. Lett.* **50**, 1092 (1987).
12. C. A. Kukkonen, S. D. Gunapala, S. V. Bandara, J. K. Liu, and J. Llorens, *Proc. SPIE* **3698**, 706 (1999).
13. S. D. Gunapala, S. V. Bandara, J. K. Liu, W. Hong, E. M. Luong, J. M. Mumolo, M. J. McKelvey, D. K. Sengupta, A. Singh, C. A. Shott, R. Carralejo, P. D. Maker, J. J. Bock, M. E. Ressler, M. W. Werner, and T. N. Krabach, *Proc. SPIE* **3379**, 382 (1998).
14. A. Jahanzeb, C. M. Travers, D. P. Butler, Z. Çelik-Butler, and J. E. Gray, *Appl. Phys. Lett.* **70**, 3495 (1997).
15. Y. K. Tseng, K. S. Liu, J. D. Jiang, and I. N. Lin, *Appl. Phys. Lett.* **72**, 3285 (1998).
16. R. A. Wood, C. J. Han, and P. W. Kruse, *Proc. IEEE Solid State Sensor and Actuator Workshop*, 132 (1992).
17. L. Méchin, J. C. Villégier, and D. Bloyet, *J. Appl. Phys.* **81**, 7039 (1997).
18. M. J. M. E. de Neville, M. P. Bruijn, R. de Vries, J. J. Wijnbergen, P. A. J. de Korte, S. Sánchez, M. Elwenspoek, T. Heidenblut, B. Schwierzi, W. Michalke, and E. Steinbess, *J. Appl. Phys.* **82**, 4719 (1997).
19. P. L. Richards, *J. Appl. Phys.* **76**, 1 (1994).
20. K. Yanagisawa, N. Itoh, and T. Ichikawa, *Proc. SPIE* **2744**, 92 (1996).
21. M. Shoda, H. Yamada, H. Yamanaka, and K. Akagawa, *Proc. SPIE* **3436**, 184 (1998).
22. M. Chi and J. Mooney, *J. Appl. Phys.* **76**, 3028 (1994).
23. N. Sclar, *Prog. Quant. Electr.* **9**, 149 (1984).
24. A. Rogalski and J. Piotrowski, *Prog. Quant. Electr.* **12**, 87 (1988).
25. A. Rogalski, *Infrared Phys. Technol.* **40**, 279 (1999).
26. T. Tung, L. V. DeArmond, R. F. Herald, P. E. Herning, M. H. Kalisher, D. A. Olson, R. F. Risser, A. P. Stevens, and S. J. Tighe, *Proc. SPIE* **1735**, 109 (1992).
27. T. J. Lyon, J. A. Vigil, J. E. Jensen, O. K. Wu, J. L. Johnson, E. A. Fatten, K. Kosai, G. Venzer, V. Lee, and S. M. Johnson, *J. Vac. Sci. Technol. B* **16**, 1321 (1998).

28. P. Mitra, S. L. Barnes, F. C. Case, M. B. Reine, P. O'Dette, R. Starr, A. Hairston, K. Kuhler, M. H. Weiler, and B. L. Musicant, *J. Electron. Mater.* **26**, 482 (1997).

29. J. M. Arias, M. Zandian, J. G. Pasko, J. Bajaj, L. J. Kozlowski, W. E. Tennant, and R. E. de Wames, *Proc. SPIE* **2274**, 2 (1994).

30. J. D. Kim, D. Wu, J. Wojkowski, J. Piotrowski, J. Xu, and M. Razeghi, *Appl. Phys. Lett.* **68**, 99 (1996).

31. J. J. Lee, J. D. Kim, and M. Razeghi, *Appl. Phys. Lett.* **73**, 602 (1998).

32. J. D. Kim, E. Michel, S. Park, J. Xu, S. Javadpour, and M. Razeghi, *Appl. Phys. Lett.* **69**, 343 (1996).

33. F. F. Sizov, in *Infrared Photon Detectors*, edited by A. Rogalski (SPIE Press, Bellingham, WA, 1995).

34. Y. C. Chang and R. B. James, *Phys. Rev. B* **39**, 12 672 (1989).

35. B. F. Levine, G. Hasnain, C. G. Bethea, and N. Chand, *Appl. Phys. Lett.* **54**, 2704 (1989).

36. S. D. Gunapala and K. M. S. V. Bandara, *Physics of Thin Films* (Academic, New York, 1995), Vol. 21, p.113.

37. B. F. Levine, A. Zussman, S. D. Gunapala, M. T. Asom, J. M. Kuo, and W. S. Hobson, *J. Appl. Phys.* **72**, 4429 (1992).

38. W. A. Beck, *Appl. Phys. Lett.* **63**, 3589 (1993).

39. M. Z. Tidrow, W. A. Beck, W. W. Clark, H. K. Pollehn, J. W. Little, N. K. Dhar, R. P. Leavitt, S. W. Kennerly, D. W. Beekman, A. C. Goldberg, and W. R. Dyer, *Proc. SPIE* **3629**, 100 (1999), and references therein.

40. L. Lunqvist, Y. J. Andersson, Z. F. Paska, J. Borglind, and D. Haga, *Appl. Phys. Lett.* **63**, 3361 (1993).

41. G. Sarusi, B. F. Levine, S. J. Pearton, S. V. Bandara, and R. E. Liebenguth, *Appl. Phys. Lett.* **64**, 960 (1994).

42. C. J. Chen, K. K. Choi, W. H. Chang, and D. C. Tsui, *Appl. Phys. Lett.* **71**, 3045 (1997).

43. W. E. Tennant, L. J. Kozlowski, W. V. McLevige, D. D. Edwall, and C. Cabelli, *Proc. IRIS Specialty Group Meeting on Infrared Detectors* (Monterey, CA, 1997).

44. M. Sundaram, T. Faska, S. Wang, A. Reisinger, M. Taylor, R. Williams, K. Zabierek, R. O. D. Burrows, D. Walker, S. Wade, S. Duvall, R. Yanka, K. Nichols, A. Vera, D. Bingham, C. Cooke, J. Roussis, M. Winn, J. Ahearn, G. Milne, K. Brown, R. Martin, K. Reiff, and W. Spahr, *Proc. IRIS Specialty Group Meeting on Infrared Detectors* (Boulder, CO, 1998).

45. M. Z. Tidrow, X. Jiang, S. S. Li, and K. Bacher, *Appl. Phys. Lett.* **74**, 1335 (1999).

46. M. Razeghi, *MOCVD Challenge Vol. 2* (Institute of Physics Publishing, Bristol, 1995).

47. M. Hasse, M. Hafich, and G. Robinson, *Appl. Phys. Lett.* **58**, 616 (1991).

48. M. Razeghi, M. Defour, F. Ohmnes, M. Dobers, J. Vieren, Y. Guldner, *Appl.Phys.Lett.* **55**, 457 (1989).

49. J.M. Olson, R.K. Ahrenkiel, D.J. Dunlavy, B. Keyes, and A.E. Kibbler, *Appl.Phys.Lett.* **55**, 1208 (1989).

50. W.C. Mitchel, G.J. Brown, K. Lo, S. Elhamri, M. Ahoujja, K. Ravindran, R. Newrock, X. He, M. Razeghi, *Appl.Phys.Lett.* **65**, 1578 (1994).

51. S. Andrews and B. Miller, J.Appl.Phys. **70**, 993 (1991).

52. R.H.Dicke and J.P.Wittke, *Introduction to Quantum Mechanics.* London, UK: Addison-Wiley (1960).

53. W. L. Wolfe and G. J. Zeiss, *The Infrared Handbook,* (Environmental Research Institute of Michigan, Ann Arbor, MI, 1985).

54. K.F. Brennan, P. Chiang, *J. Appl. Phys.* **71**, 1055 (1992).

55. W.Masselink, N.Braslau, D.La Tulipe, W.Wang, and S.Wright, *Solid-State Electron.* **31**, 337 (1988).

56. H. C. Liu, J. Li, M. Buchanan, and Z. R. Wasilweski, *IEEE J. Quantum Electron.* **32**, 1024 (1996).

57. M. J. Kane, S. Millidge, M. T. Emeny, D. Lee, D. R. P. Guy, and C. R. Whitehouse, in *Intersubband Transitions in Quantum Wells,* eds. E. Rosencher, B. Vinter, and B. Levine (Plenum, New York, 1992), pp. 31–42.

58. C. Jelen, S. Slivken, T. David, M. Razeghi, and G. J. Brown, *IEEE J. Quant. Electron.* **34**, 1124 (1998).

59. M. Razeghi, *MOCVD Challenge Vol. 1* (Adam Hilger, Bristol, 1989), pp. 8–24; M. Razeghi, *MOCVD Challenge Vol. 2* (Institute of Physics Publishing, Bristol, 1995), pp. 22–49.

60. S. L. Chuang, *Physics of Optoelectronic Devices* (John Wiley & Sons, New York, 1995), pp. 31–35.

61. M. A. Kinch and A. Yariv, *Appl. Phys. Lett.* **55**, 2093 (1989).

62. S. D. Gunapala, B. F. Levine, L. Pfeiffer, and K. West, *J. Appl. Phys.* **69**, 6517 (1991).

63. G. Hasnain, B. F. Levine, S. Gunapala, and N. Chand, *Appl. Phys. Lett.* **57**, 608 (1990).

64. S.J. Chua and A. Ramam, *Proceedings of the 1996 IEEE International Conference on Semiconductor Electronics, ISDE.* Piscataway, NJ: SPIE Press. pp.469-471, 1994.

65. S. D. Gunapala, B. F. Levine, D. Ritter, R. A. Hamm, and M. B. Panish, *Appl. Phys. Lett.* **60**, 636 (1992).

66. T. Fujii, Y. Nakata, Y. Sugiyama, and S. Hiyamizu, *Jpn. J. Appl. Phys.* **25**, Pt.2, No. 3, L254-L256 (1986).

67. D. Olego, T.Y. Chang, E. Silberg, E.A. Caridi and A. Pinkzuk, *Appl. Phys. Lett.* vol. **41**, No. 5, pp. 476-478, Mar. 1982.

68. T. Ishikawa and J.E. Bowers, *IEEE J. Quant. Electron.* vol. **30**, No. 2, pp. 562-570, Feb. 1994.

69. W.A. Harrison, *J. Vac. Sci. Technol.* vol. **14**, No. 4, pp. 1016-1021, July/Aug. 1977.

70. Y.Kawamura, H. Kobayahsi, and H. Iwamura, *Jpn. J. Appl. Phys.* vol. **33 Pt. 2: Letters,** No. 1B, pp. L79-L82, Feb. 1994.

71. A.Rose, *Concepts in photoconductivity and allied problems.* NY: John Wiley & Sons, (1963).

72. D.Wang, Y.Wang, G.Bosman, S.Li, *Noise in Physical Systems and 1/f Fluctuations,* AIP Conf. Proc. p.415 (1993).

73. D.Wang, G.Bosman, Y.Wang, S.Li, *J.Appl.Phys.* **77**, 1107 (1995)

74. Aldert van der Ziel, *Noise in solid state devices and circuits.* NY: John Wiley & Sons, (1986).

75. R. H. Bube, *Photoelectrical properties of semiconductors.* Cambridge, UK: Cambridge university press, (1992).

76. L. T. Claiborne and M. A. Dodd, *Proc. SPIE* **2999**, 32 (1997).

77. S. D. Gunapala, B. F. Levine, D. L. Silco, and A. Y. Cho, *Appl. Phys. Lett.* **56**, 770 (1990).

78. S.D. Gunapala, J.K. Liu, J.S. Park, M. Sundaram, C.A. Shott, T. Hoelter, T. Lin, S.T. Massie, P.D. Maker, R.E. Muller, G. Sarusi, *IEEE transactions on electron devices* **44**, 51-57. (1997).

79. B. Soucail, P. Voisin, M. Voos, D. Rondi, J. Nagle, and B. de Crémoux, *Semicond. Sci. Tech.* **5**, 918 (1990).

80. R. E. Cavicchi, D. V. Lang, D. Gershoni, A. M. Sargent, J. M. Vandenberg, S. N. G. Chu, and M. B. Panish, *Appl. Phys. Lett.* **54**, 739 (1989).

81. D. L. Mathine, *IEEE J. Select. Top. Quant. Electron.* **3**, 952 (1997).

82. M. Razeghi, R. Sudharsanan, and J. C. C. Fan, *Proc. International Conference on Solid State Devices and Materials* (Tsukuba, Japan, 1992), p. 622.

83. D. K. Sengupta, W. Feng, J. I. Malin, J. Li, T. Horton, A. P. Curtis, K. C. Hsieh, S. L. Chuang, H. Chen, M. Feng, G. E. Stillman, L. Li, H. C. Liu, K. M. S. V. Bandara, S. D. Gunapala, and W. I. Wang, *Appl. Phys. Lett.* **71**, 78 (1997).

84. E. R. Brown, F. W. Smith, G. W. Turner, K. A. McIntosh, and M. J. Manfra, *Proc. SPIE* **1735**, 228 (1992).

85. J. W. Matthews and A. E. Blakeslee, *J. Cryst. Growth* **27**, 118 (1974).

86. R. People and J. C. Bean, *Appl. Phys. Lett.* **47**, 322 (1985).

87. P. Bhattacharya, *Semiconductor Optoelectronic Devices*, (Prentice Hall, Englewood Cliffs, NJ, 1994).

88. E. A. Beam III and Y. C. Kao, *J. Appl. Phys.* **69**, 4253 (1991).

89. S. Luryi and E. Suhir, *Appl. Phys. Lett.* **49**, 140 (1986).

90. E. A. Fitzgerald, P. D. Kirchner, R. Proano, G. D. Pettit, J. M. Woodall, and D. G. Ast, *Appl. Phys. Lett.* **52**, 1496 (1988).

91. J. W. Matthews, S. Mader, and T. B. Light, *J. Appl. Phys.* **41**, 3800 (1970).

92. L. Buydens, P. Demeester, M. Van Ackere, A. Ackaert, and P. Van Daele, *J. Electron. Mater.* **19**, 317 (1990).

93. O. Kayser, *J. Cryst. Growth* **107**, 989 (1991).